Fatigue behavior of powder bed Fused–Laser beam (PBF-LB) 70/30 Copper-Nickel (CuNi30)

International Journal of Fatigue 208 (2026) 109574

Contents lists available at ScienceDirect

International Journal of Fatigue

journal homepage: www.elsevier.com/locate/ijfatigue

Fatigue behavior of powder bed Fused–Laser beam (PBF-LB) 70/30 Copper-Nickel (CuNi30)

Mojtaba Roshan [a,1], MohammadBagher Mahtabi [a,1], Wiktor Bednarczyk [b], Marta Gajewska [c], Grzegorz Cios [c], Alessandro Benelli [d], Andrea Tridello [e,f], Zaynab Mahbooba [g], Ankit Saharan [g], Meysam Haghshenas [a,*]

[a] Fatigue, Fracture, and Failure Laboratory (F3L), College of Engineering, University of Toledo, OH 43606, USA
[b] Faculty of Metals Engineering and Industrial Computer Science, AGH University of Kraków, Kraków, Poland
[c] Academic Centre for Materials and Nanotechnology, AGH University of Kraków, Kraków, Poland
[d] Department of Applied Science and Technology, Politecnico di Torino, Turin, Italy
[e] Department of Mechanical and Aerospace Engineering, Politecnico di Torino, Turin, Italy
[f] Inter-Departmental Multi-Disciplinary Research Centre J-TECH @PoliTO, Turin, Italy
[g] EOS North America Inc., Pflugerville, TX 78660, USA

ARTICLE INFO

Keywords:
70/30 Cu–Ni
CuNi30
Additive manufacturing
Powder bed fused–laser beam
Fatigue
Facet

ABSTRACT

The 70/30 Cu–Ni alloy (CuNi30) is widely employed in marine systems due to its excellent corrosion resistance and mechanical reliability. Despite its industrial relevance, its behavior under additive manufacturing (AM), particularly powder bed fusion–laser beam (PBF-LB) processing, has received limited attention in the context of fatigue-critical applications. This study presents the first systematic assessment of the microstructure, defect population, mechanical properties, and fatigue performance of PBF-LB 70/30 Cu–Ni in both the as-built and heat-treated conditions, with specific attention to the role of build orientation using horizontally and vertically fabricated specimens. The applied heat treatment increased mechanical strength and produced a marked improvement in the stress–life (S–N) response of the alloy. Detailed microstructural characterization and post-mortem fractography showed that fatigue cracks predominantly initiated from surface or subsurface crystallographic facets induced by local embrittlement in the matrix. The results provide essential guidance for designing fatigue-resistant Cu–Ni components and support the broader adoption of PBF-LB 70/30 Cu–Ni in demanding marine and naval environments. Furthermore, this work establishes a foundation for future investigations into the corrosion-fatigue behavior of the alloy.

1. Introduction

Copper–nickel alloys, commonly known as cupronickels, are renowned for their excellent corrosion resistance, high strength, and superior workability. Among them, 70/30 Cu–Ni (70% copper, 30% nickel) is especially valued for its exceptional resistance to seawater corrosion, biofouling, and erosion, attributes that make it highly valuable for marine engineering applications [1–3]. The alloy's unique combination of copper's ductility and nickel's strengthening effect ensures mechanical stability and long-term reliability in harsh, high-salinity environments. Consequently, 70/30 Cu–Ni is widely employed in heat exchangers, condensers, seawater piping, and propulsion systems, where components are frequently exposed to cyclic stresses arising from mechanical loading, pressure fluctuations, and temperature variations [4–6]. Understanding the fatigue behavior of 70/30 Cu–Ni is therefore essential for predicting component lifespan and preventing premature failures that could result in significant economic losses, safety hazards, and environmental impacts. Moreover, detailed insight into its fatigue properties allows for improved material selection and optimized fatigue-critical design.

Considering the complex geometries often required in components fabricated from Cu–Ni alloys for the mentioned applications, powder-based additive manufacturing (AM) techniques, especially powder bed fusion – laser beam (PBF-LB), have significantly expanded the manufacturability of these alloys compared with conventional processing

* Corresponding author.
E-mail address: meysam.haghshenas@utoledo.edu (M. Haghshenas).
[1] Equal contribution .

https://doi.org/10.1016/j.ijfatigue.2026.109574
Received 15 December 2025; Received in revised form 5 February 2026; Accepted 12 February 2026
Available online 17 February 2026

Nomenclature

a	Basquin Constant
AB	As-Built
AM	Additive Manufacturing/ Additively Manufactured
ASTM	American Society for Testing and Materials
b	Basquin Exponent
BC	Band Contrast
BSE	Backscattered
EBSD	Electron Backscatter Diffraction
EBSP	Electron Backscatter Pattern
EDS	Energy-Dispersive X-Ray Spectroscopy
FCC	Face-Centered Cubic
FE-SEM	Field Emission Scanning Electron Microscope
FGA	Fine-Grained Area
GNDs	Geometrically Necessary Dislocations
HAADF-STEM	High-Angle Annular Dark-Field Scanning Transmission Electron Microscopy
HAGBs	High-Angle Grain Boundaries
HCF	High-Cycle Fatigue
HT	Heat Treated
HV	Vickers hardness
IPF	Inverse Pole Figure
KAM	Kernel Average Misorientation
LAGBs	Low-Angle Grain Boundaries
LCF	Low-Cycle Fatigue
LoF	Lack of Fusion
MRD	Multiples of Random Distribution
N_f	Number of Cycles to Failure
PF	Pole Figure
PSB	Persistent slip band
PSD	Particle Size Distribution
R	Stress Ratio
SEM	Scanning Electron Microscopy
S-N	Stress Amplitude *vs.* Number of Cycles to Failure
TEM	Transmission Electron Microscopy
XCT	X-ray Computed Tomography
XRF	X-ray Fluorescence

routes. However, the very nature of PBF-LB introduces challenges for achieving predictable and consistent mechanical properties, particularly in terms of fatigue performance [7–9]. During fabrication, the localized and repeated heating and cooling cycles in PBF-LB create complex thermal gradient histories within the material, often leading to the development of residual stresses in the printed parts [10–12]. These stresses can significantly influence mechanical behavior, potentially accelerating fatigue crack initiation or altering crack growth paths [13,14]. To mitigate such effects, post-processing heat treatment (HT) is commonly applied to reduce residual stress levels and stabilize the microstructure [15,16].

One of the most critical challenges associated with PBF-LB components is the presence of microstructural defects (e.g., local segregation) and/or volumetric defects (e.g., gas porosities and lack of fusion defects), which serve as potent stress concentrators and can substantially degrade structural integrity [17–19]. Such imperfections are especially detrimental under cyclic loading, where fatigue failure often initiates at these inevitable defects [20–23]. Furthermore, build orientation introduces an additional level of complexity, as it governs both the spatial distribution of defects and the resulting anisotropy in mechanical properties [24,25]. Numerous studies have examined the effects of build orientation, residual stress, and AM-caused defects, highlighting that their interplay can significantly alter fatigue performance [26–29]. Understanding and controlling these interconnected, material-dependent factors is therefore essential for improving the reliability and service life of AM parts in demanding applications.

In recent years, some studies have investigated the microstructure and mechanical properties of PBF-LB 70/30 Cu–Ni (also known as CuNi30), with particular focus on its tensile and corrosion performance [30–34]. Nadimi et al. [30] investigated the microstructure and corrosion behavior of LPBF-fabricated 70/30 Cu–Ni and reported that all AB samples exhibited surface porosity, although the porosity percentage remained below 1 %, reflecting a highly dense as-printed material with minimal pore presence. They also observed that the grains in the as-fabricated condition were generally larger, exhibiting elongated, irregular shapes with a preferred orientation along the <101> crystallographic direction. Liu et al. [31] examined the tensile properties of PBF-LB 70/30 Cu–Ni and reported that the printed specimens exhibited superior mechanical properties and corrosion resistance compared to their commercial counterpart. Grain refinement, combined with dislocation tangles and high density of dislocations, was found to contribute to the enhanced tensile strength and ductility of the PBF-LB alloy. Gao et al. [32] introduced Nb and C into PBF-LB CuNi30 and demonstrated that this addition promotes in situ NbC formation, thereby enabling dual-scale strengthening due to the presence of micron-scale NbC particles and nano-scale NbC precipitates. Recently, Anjum et al. [33] reported the tensile behavior of PBF-LB CuNi30 in both the AB and post–HT (550°C for 2h) conditions and observed notable increases in yield stress (YS) and ultimate tensile strength (UTS) following HT, consistent with the trends previously observed by Roshan et al. [34].

The existing literature on the fatigue behavior of 70/30 Cu–Ni is restricted to conventionally manufactured counterparts, such as cast or wrought alloys [35,36]. However, AM-processed 70/30 Cu–Ni is expected to exhibit markedly different fatigue performance due to the intrinsic characteristics of AM (e.g., PBF-LB). To the best of the authors' knowledge, no prior study has systematically examined the fatigue performance of PBF-LB processed 70/30 Cu–Ni alloys, and several open questions remain regarding the influence of build orientation, defect characteristics, and post-printing HT on the alloy's fatigue response, as well as the associated governing mechanisms of fatigue crack behavior, including crack initiation and early-stage propagation. The unique microstructural features introduced by PBF-LB, such as anisotropic grain structures, heterogeneous defect distribution, and localized compositional variations, can strongly influence the fatigue crack initiation and propagation mechanisms. This knowledge gap implies an urgent need for a comprehensive and systematic investigation into the fatigue behavior of PBF-LB 70/30 Cu–Ni, particularly to establish the alloy's reliability in applications where resistance to cyclic loading is dominant.

This study, therefore, aims to evaluate the microstructure and mechanical properties of PBF-LB 70/30 Cu–Ni, with a particular emphasis on its fatigue behavior. To this end, specimens were produced in two different build orientations (horizontal and vertical), and half of them underwent a post-printing HT to mitigate the potential influence of residual stresses generated during fabrication. Porosity analysis was performed to quantify process-induced defects and assess their potential impact on fatigue performance. Furthermore, both pre- and post-mortem advanced microstructural and fractography characterizations were conducted to establish correlations between fatigue fracture characteristics and underlying microstructural features to quantify controlling mechanism(s) of fatigue crack behavior. Given that this alloy is ultimately intended for deployment in corrosive environments where cyclic loading is simultaneously present (e.g., various naval applications), the present focus on its ambient-air fatigue response in this research provides a necessary and rigorous baseline for future investigations into the corrosion-fatigue behavior of the PBF-LB 70/30 Cu–Ni.

Table 1
Chemical composition (wt.%) of the studied 70/30 Cu–Ni alloy produced by PBF-LB. For the sake of comparison, the ASTM B369 specification for C96400 is also provided.

Specimen ID	Cu	Ni	Fe	Mn	Nb	Si
C96400 (B369)	Balance	28–32	0.25–1.5	1.5 max	0.5–1.5	0.5 max.
Studied alloy	66.566	30.376	1.052	1.053	0.787	0.166

2. Experimental procedure

2.1. Specimen fabrication and preparation

In this research, 70/30 Cu–Ni specimens were fabricated using the PBF-LB process on an EOS M400 system. Gas-atomized 70/30 Cu–Ni powders supplied by EOS were utilized, conforming to the ASTM B369-09 [37] chemical composition specifications for alloy C96400. Most particles were spherical in morphology, and the particle size distribution (PSD) fell within approximately 15–65μm. X-ray fluorescence (XRF) was used to verify the chemical composition of the printed specimens (Table 1).

For specimen fabrication, cylindrical rods were produced in two build orientations (vertical and horizontal; see Fig. 1a & b) using process parameters optimized by EOS to ensure highly dense components. Following the printing process, half of the specimens underwent a post-print HT cycle: soaking at 600°C for 2h in a vacuum furnace backfilled with nitrogen, followed by controlled cooling at 30°C/min. This treatment enabled direct comparison with specimens in the as-built (non-heat-treated) condition. Cylindrical rods were machined into dog-bone specimens for fatigue testing in accordance with ASTM E466 [38]. It is worth noting that, in the present study, long bars were fabricated in both horizontal and vertical build orientations for high-cycle fatigue (HCF) testing. These bars were subsequently machined into ASTM E466 dog-bone fatigue specimens (the gauge diameter and gauge length are shown in Fig. 1c). In addition, short bars (also printed in both orientations) were included on the same build plate for a planned follow-on study requiring shorter hourglass specimens. Printing both long and short bars in a single build was carried out to improve manufacturing efficiency.

Accordingly, four specimen groups were prepared for this study:
(*i*) Vertically printed as-built (AB) specimens,
(*ii*) Horizontally printed as-built (AB) specimens,
(*iii*) Vertically printed heat-treated (HT) specimens,
(*iv*) Horizontally printed heat-treated (HT) specimens.

2.2. Microstructure and defect characterizations

The characterization was carried out on a Thermo-Fisher Scientific Helios 5 field-emission scanning electron microscope (FE-SEM), which was equipped with an Oxford Instruments Symmetry S3 electron backscatter diffraction (EBSD) detector. Backscattered electron (BSE) imaging was conducted at 10kV in high-resolution scanning electron

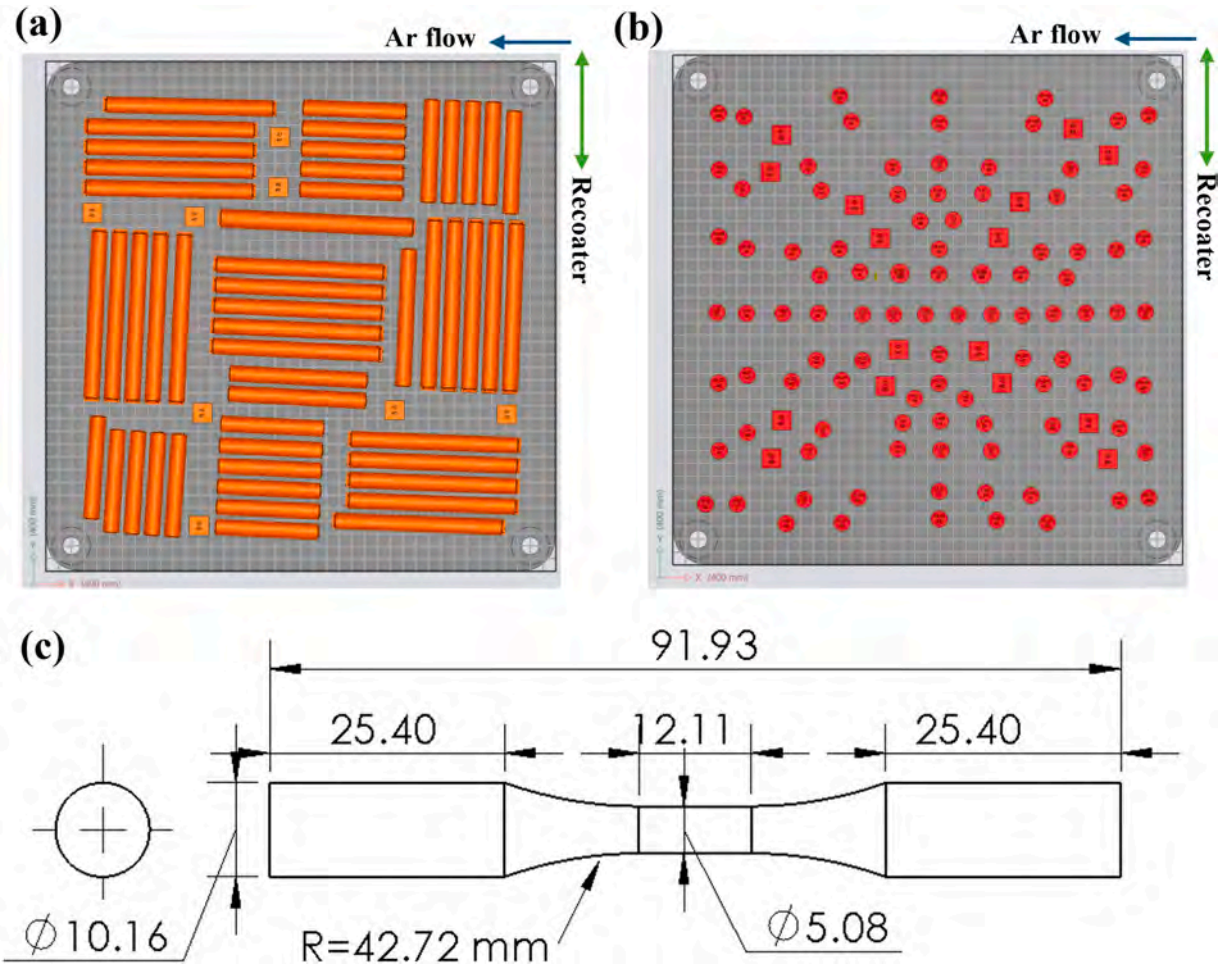

Fig. 1. (a) horizontally printed cylindrical rods, (b) vertically printed cylindrical rods, and (c) machined specimen configurations, along with their dimensions (in mm).

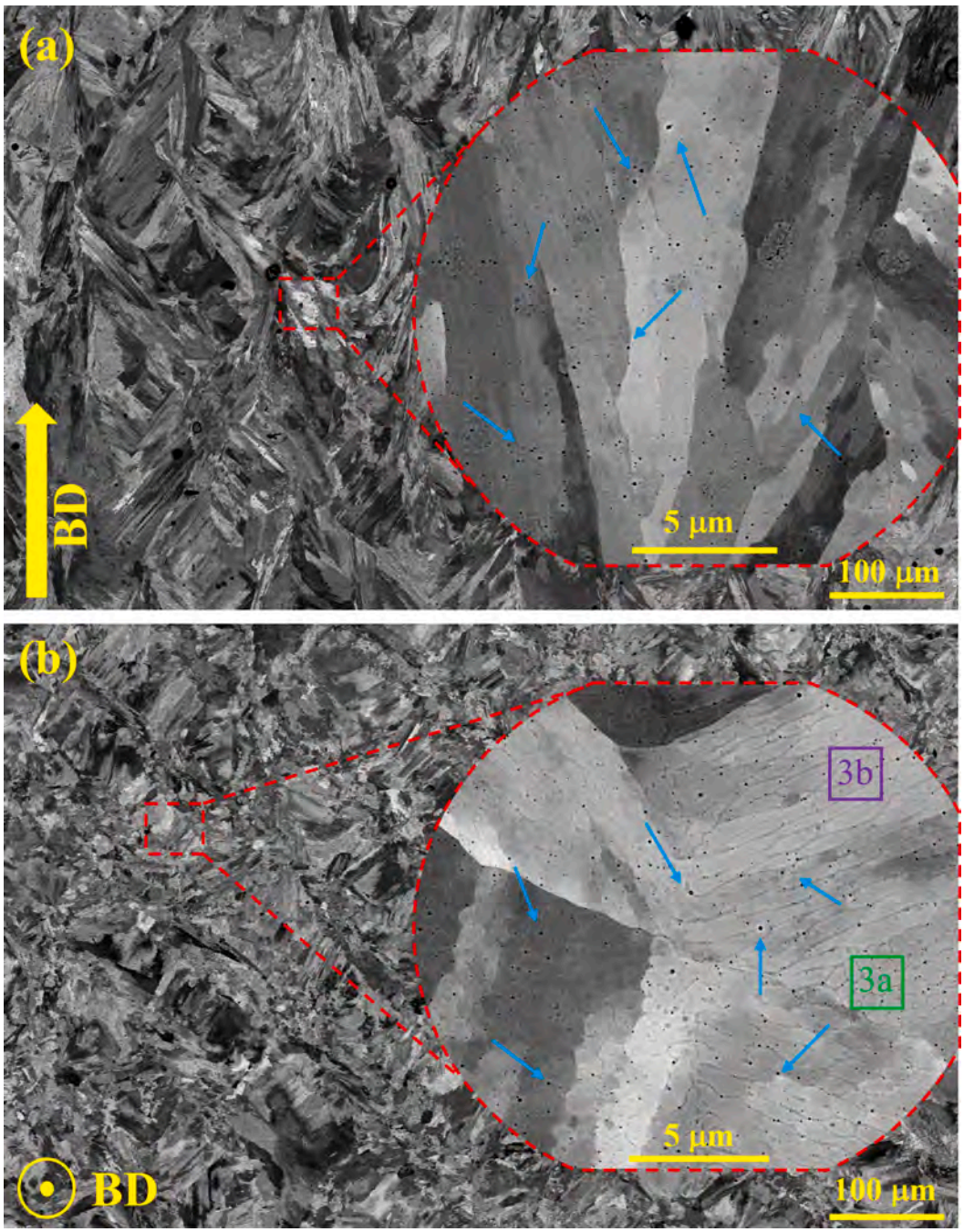

Fig. 2. SEM-BSE of the 70/30 Cu–Ni alloy in the AB state, (a) YZ plane and (b) XY plane.

microscopy (SEM) mode, while EBSD data were acquired at 20kV. Electron backscatter patterns (EBSP) were processed using the Hough transform, successfully indexing only the Cu-based face-centered cubic (FCC) phase (a=0.361nm), as the resolution was insufficient to detect fine secondary-phase grains. Samples for SEM and EBSD analysis were prepared by conventional metallographic grinding and polishing, followed by 15-minute vibratory polishing.

Grain boundaries were categorized based on their misorientation angle. Low-angle grain boundaries (LAGBs) were defined by misorientation angles ranging from 3° to 15° (represented by gray lines), while high-angle grain boundaries (HAGBs) spanned the range of 15° to 63° (represented by black lines). For a boundary to be considered a valid grain boundary, it requires a cluster of at least five points exhibiting a misorientation greater than 15°. Grain size was calculated using the weighted average equivalent circle diameter method. Crystallographic texture was characterized by generating inverse pole figures (IPFs), pole figures (PFs), and grain size distribution plots with the aid of the ATEX software package [39].

To investigate nanoscale features and local chemical composition, transmission electron microscopy (TEM) was carried out using a FEI Tecnai G2 F20 (FEG) microscope equipped with an energy-dispersive X-ray (EDX) detector. Local elemental distributions were further characterized using a Themis probe-corrected TEM with a Super-X quad Energy-dispersive X-ray spectroscopy (EDS) detector (Thermo-Fisher Scientific). TEM analyses were conducted at 200kV. Bright-field (BF) imaging and scanning TEM (STEM) with a high-angle annular dark-field (HAADF) detector were employed. EDX was used for both point/area composition measurements and elemental mapping. Thin foils were

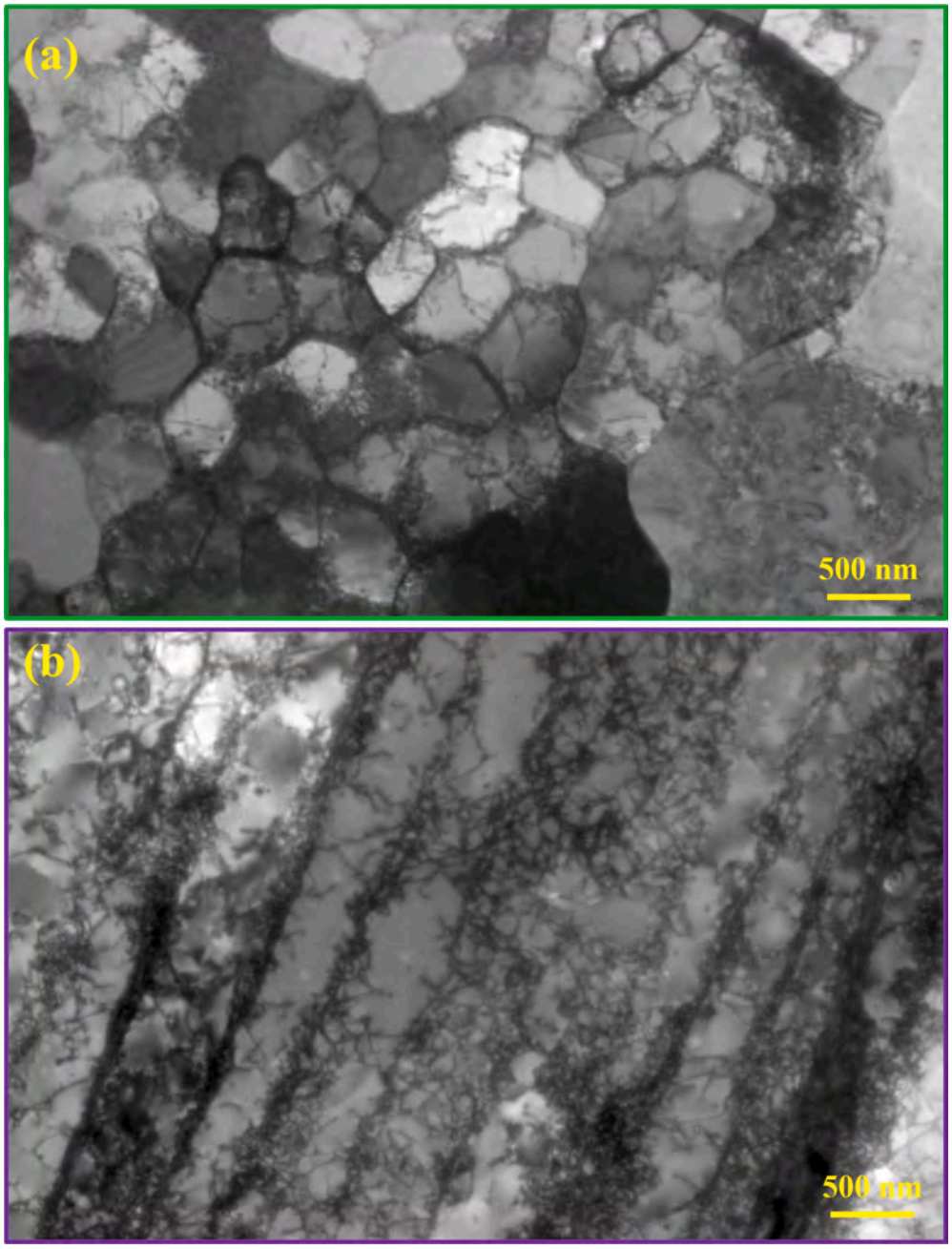

Fig. 3. TEM graphs of the (a) equiaxed cells (green box in Fig. 2), and (b) lamellar cells (purple box in Fig. 2).

prepared with a Tenupol-5 (Struers) double-jet electro-polisher using an electrolyte of nitric acid and methanol (3:7), at 233K and 20V. For both AB and HT conditions, foils were sectioned perpendicular to the build direction (XY).

In addition, process-induced defects were quantitatively assessed using a custom X-ray computed tomography (XCT) system, equipped with a 50W X-ray tube and a minimum focal spot size of 5μm, with all specimens inspected over an approximately 10mm-long central gauge region. The specimens were inspected in the central region, and the acquisition parameters were 290kV and 160 μA, corresponding to a nominal power of 46.4W. A spatial resolution of 5.4μm was achieved by setting a source-to-specimen distance of 35mm and a source-to-detector distance of 1300mm. To avoid quantification near the voxel-size resolution limit, a conservative minimum-size criterion was imposed. Specifically, only defects exceeding a voxel-grid–defined threshold were retained, corresponding to a minimum detectable radius of approximately three times the voxel size. This threshold lies above the nominal resolution limit of the XCT system. Defects smaller than this limit were excluded to prevent unreliable measurements associated with resolution-limited features.

For each specimen, 1600 2D projections were acquired, and the 3D reconstruction was performed using VG MAX 3.5 software (Volume Graphics GmbH, Heidelberg, Germany) with a filtered back-projection algorithm. A 1mm-thick copper filter was used to remove low-energy radiation and enhance the final quality of the reconstructions. The defect distribution was characterized using the VG Studio inclusion/porosity module. This study focused on evaluating the projected area of each defect in the plane orthogonal to the vertical axis of the specimens and the equivalent diameter.

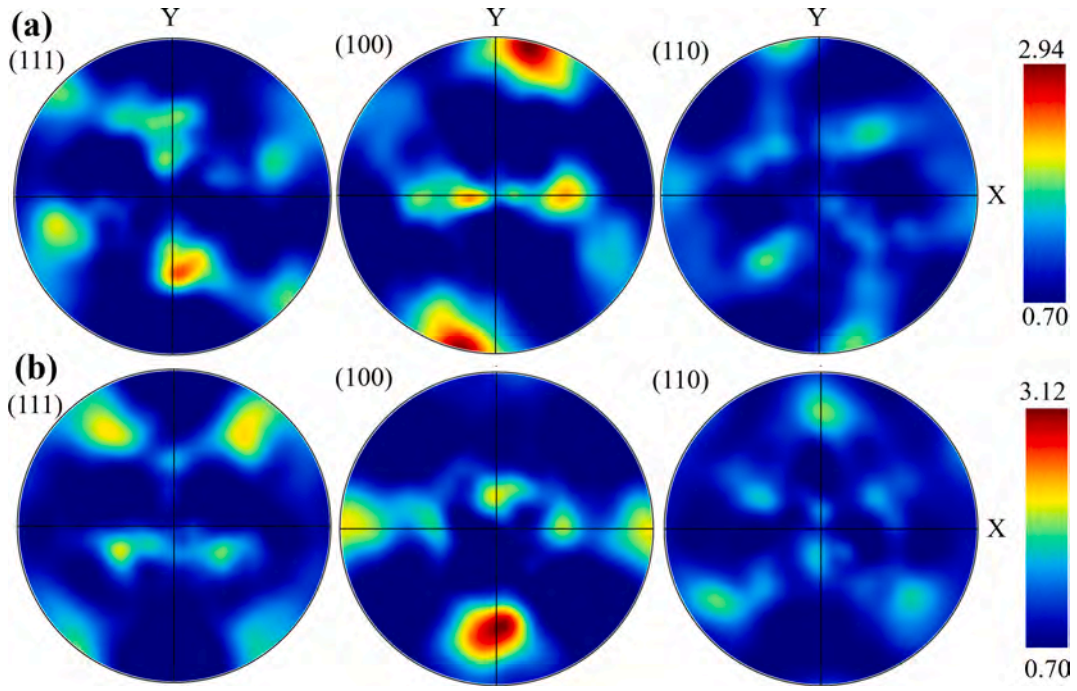

Fig. 4. Pole figures of vertically printed PBF-LB 70/30 Cu–Ni showing the crystallographic texture along the build direction (Z-axis); (a) AB state, and (b) HT condition.

2.3. Tensile and fatigue tests

The mechanical properties of the material were evaluated through quasistatic uniaxial tensile testing to quantify its strength and ductility. All tests were conducted at ambient temperature under strain-controlled loading in accordance with the ASTM E8/E8M guidelines [40], using a nominal strain rate of 10^{-3} s^{-1}. An Instron Model 1332 universal testing system equipped with a 20mm Epsilon extensometer was employed to ensure precise strain measurement. For each build orientation and processing condition (AB and HT), three replicate specimens were tested to confirm the repeatability of the mechanical response.

Fatigue response of the studied material was evaluated through uniaxial fatigue tests conducted at room temperature using an MTS servo-hydraulic load frame. Force-controlled fatigue tests were performed under fully reversed loading (R = –1) with a sinusoidal waveform and cyclic frequency of 10Hz, in accordance with ASTM E466 [38]. Following fatigue testing, fracture surfaces and subsurface regions perpendicular to the fracture plane were examined using optical microscopy (Keyence VHX6000) and an ultra-high-resolution FEI Quanta 3D FEG SEM equipped with EBSD to characterize fatigue failure mechanisms.

3. Results and discussion

3.1. Characterization of starting microstructure

SEM micrographs were obtained from planes both perpendicular and parallel to the build direction for all PBF-LB 70/30 Cu–Ni groups (i.e., AB and HT). The analysis revealed that the microstructures, in terms of grain size, morphology, and subgrain features, were largely consistent across all groups. Therefore, to avoid redundancy, Fig. 2 presents the representative microstructure of the vertically printed AB sample. A more comprehensive analysis of the PBF-LB 70/30 Cu–Ni microstructure is detailed in our previous work [34].

On planes parallel to the build direction (Fig. 2a), the microstructure was characterized by columnar grains elongated along this axis. This morphology is a direct consequence of directional solidification, where grains grow epitaxially along the maximum thermal gradient. In contrast, planes perpendicular to the build direction (Fig. 2b) revealed the cross-sections of these columnar grains, which presented a nearly equiaxed appearance. This difference is significant when evaluating the build orientation of fatigue specimens: in vertically printed specimens, elongated grains align parallel to the loading axis, while in horizontally printed specimens, they align perpendicular to it. Such orientation-dependent alignment directly influences the anisotropic mechanical response of the material.

At higher magnification, a multi-scale, hierarchical sub-structure was observed within the grains. The presence of these hierarchical features reflects the strong influence of the thermal gradient during solidification and underscores the inherent complexity of microstructures generated by PBF-LB processing [41,42]. The extreme undercooling experienced during rapid solidification can induce instabilities at the solid–liquid interface, leading to the development of fine cellular substructures with submicron-scale features within the grains (see TEM images in Fig. 3). These lamellar and equiaxed cellular structures are characterized by dislocation-rich cell boundaries. These boundaries form a dense network that likely contributes to strengthening the alloy by impeding dislocation motion. Such cells indicate local variations in solidification conditions and thermal gradients during the layer-wise PBF-LB process. Furthermore, dark contrast features observed in high-magnification BSE micrographs (indicated by blue arrows in Fig. 2) were predominantly distributed along grain and subgrain boundaries. Given their distribution and imaging contrast, these regions are more likely to be silicon-rich oxide particles (e.g., SiO_2) formed during processing.

Fig. 4 presents the pole figure (PF) maps of vertically printed PBF-LB 70/30 Cu–Ni samples in both as-built (AB) and heat-treated (HT) conditions. Texture analysis along planes parallel to the build direction, as shown in the PF maps and the corresponding calculated pole figures, reveals a moderate texture intensity with a preferred <100> grain orientation. The alignment of <100> grains along the build direction is a characteristic feature commonly observed in additively manufactured alloys.

Fig. S1 (Supplementary Materials) presents bar charts of grain size

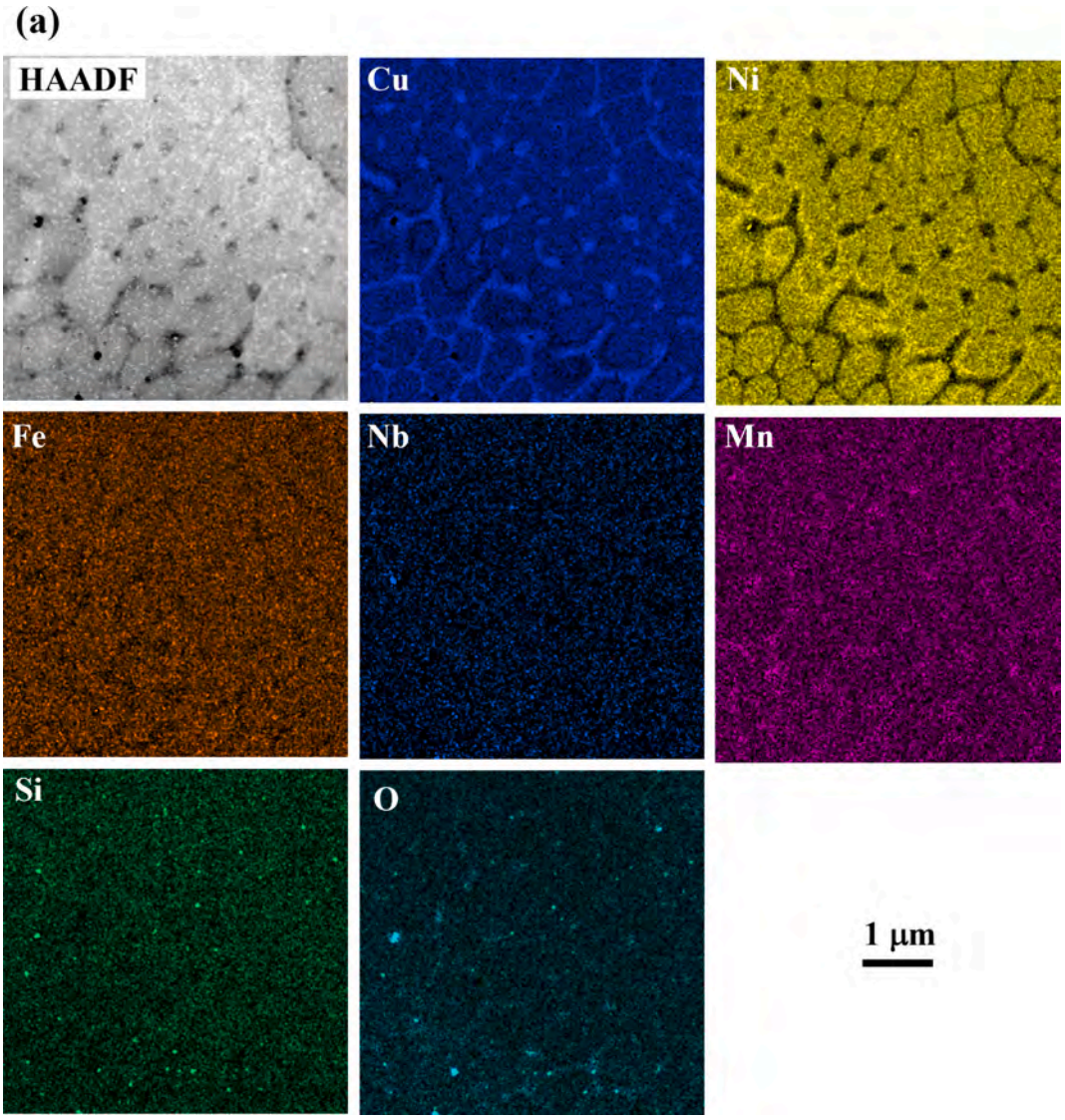

Fig. 5. HAADF-STEM images with corresponding elemental mapping of the studied 70/30 Cu–Ni: (a) AB condition, and (b) HT condition.

distribution for a horizontally built PBF-LB 70/30 Cu–Ni specimen in both the AB and HT conditions, shown for the XY and XZ planes (perpendicular and parallel to the loading direction, respectively). As seen in Fig. S1(a), in the XY plane, HT does not produce any noticeable change in the grain size distribution. This result is expected, since the primary purpose of HT was to relieve residual stresses from the AB state without causing significant grain growth. In contrast, for the XZ plane (Fig. S1(b)), a slight reduction in the number of fine grains is observed, although the overall change remains marginal.

To characterize the phase composition and solute distribution, TEM analyses were performed on PBF-LB 70/30 Cu–Ni samples in both the AB and HT conditions. Fig. 5 shows the HAADF-STEM images acquired for both conditions. The HAADF-STEM micrographs reveal a fine cellular substructure within the grains, characteristic of the rapid solidification associated with the PBF-LB process. The elemental maps display a uniform distribution of Cu and Ni within the cell interiors, confirming the formation of a homogeneous α-phase solid solution. In the AB condition (Fig. 5a), the cell boundaries are enriched in Cu and slightly in Mn, accompanied by a depletion of Ni, indicating non-equilibrium solute segregation caused by rapid cooling. In contrast, the HT condition (Fig. 5b) exhibits a much weaker segregation pattern, and Cu enrichment at cell boundaries is less pronounced than in the AB condition, suggesting that HT promotes partial homogenization through diffusion. For both conditions, no significant segregation of Si or Nb was detected between the cell interiors and boundaries.

Additionally, co-localization of Si and O observed in the elemental maps confirms the presence of nanoscale silicon oxide (likely SiO_2) inclusions, which are distributed within grains and along cell boundaries. These oxides are attributed to reactions between silicon and residual oxygen, either present in the processing chamber atmosphere or adsorbed on the powder feedstock surface before melting.

3.2. AM-induced volumetric defects

Internal defects in the fatigue specimens were characterized using XCT. Process-induced defects, including gas porosity and lack of fusion, act as stress concentrators and serve as preferential sites for fatigue crack initiation, thereby significantly reducing the overall fatigue life of the component.

To ensure high-resolution analysis of the most critical region, the scans were focused on the gauge section of the fatigue specimens. Although HT at 600°C for 2h can relieve residual stress and modify defect morphology, substantial changes in pore distribution are generally not expected at this temperature and duration. The defect

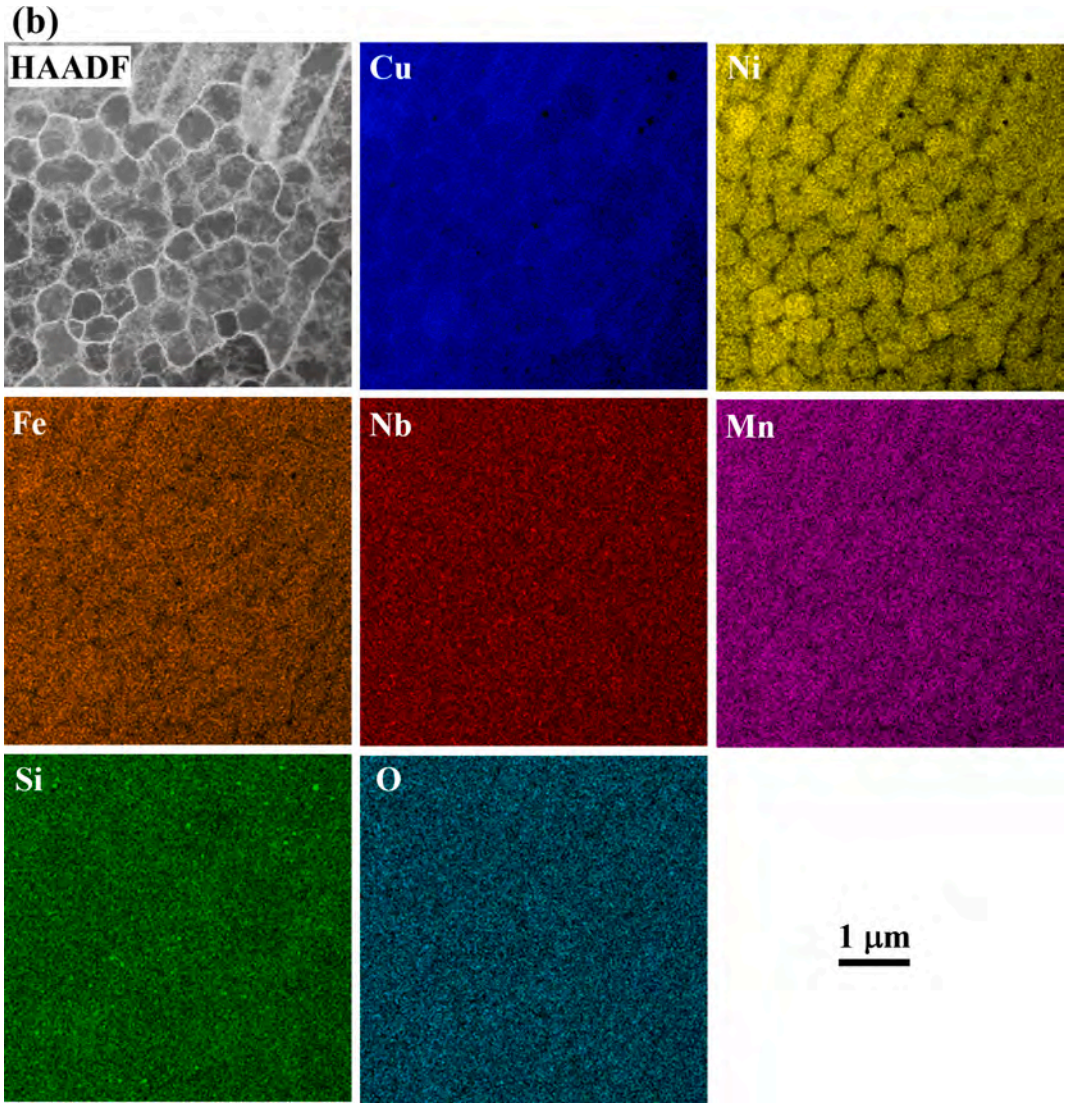

Fig. 5. (*continued*).

Table 2
Summary of XCT results for the PBF-LB 70/30 Cu–Ni fatigue specimens in different conditions (total scan volume: 200mm^3).

	V-AB	H-AB	V-HT	H-HT
Total defect volume (μm^3)	6.29E+5	8.65E+5	2.97E+6	1.71E+6
Largest volume of defects (μm^3)	8.10E+4	7.90E+4	1.10E+5	1.70E+5
Average volume of defects (μm^3)	5.93E+3	6.00E+3	1.58E+4	7.97E+3
largest surface area of defects in XY plane (μm^2)	3.44E+3	2.70E+3	1.94E+3	3.97E+3
Average surface area of defects in XY plane (μm^2)	4.16E+2	4.04E+2	9.54E+2	4.68E+2

V-AB: vertically printed (as-built).
H-AB: horizontally printed (as-built).
V-HT: vertically printed (post heat treated).
H-HT: horizontally printed (post heat treated).

characteristics for all four conditions (vertically printed AB, horizontally printed AB, vertically printed HT, and horizontally printed HT) are quantitatively summarized in Table 2. For defect quantification, the XY plane was defined locally for each specimen as the plane perpendicular to the applied loading direction, ensuring that projected areas correspond to sections mechanically equivalent relative to the applied stress, regardless of global build orientation.

The total defect volume was found to be higher in HT samples compared to AB samples, with the vertically printed HT specimen exhibiting the largest total defect volume (2.97×10^6 μm^3). The largest individual defect was observed in the horizontally printed HT specimen (1.70×10^5 μm^3), while the average defect volume was greatest in vertically printed HT samples (1.58×10^4 μm^3). Defect surface area analysis further revealed that the horizontally printed HT specimens contained defects with the largest projected areas in the XY plane (3.97×10^3 μm^2). These defects are expected to play a critical role in reducing fatigue life, as large surface-connected or planar defects can act as preferential crack initiation sites under cyclic loading. These larger defects in horizontally printed HT specimens reduce the effective load-bearing cross-section and generate local stress concentrations, promoting early crack nucleation under cyclic loading and contributing to the higher scatter in fatigue data.

Representative XCT reconstructions are presented in Fig. 6. The largest defects, measured by equivalent diameter, were 53μm and 69μm for the horizontally printed AB and horizontally printed HT specimens, respectively. In the vertically printed specimens, the largest defects were 56μm for vertically printed AB and 59μm for vertically printed HT. These observations suggest that neither build orientation nor post-process HT substantially affected the size or spatial distribution of the pre-existing defect population.

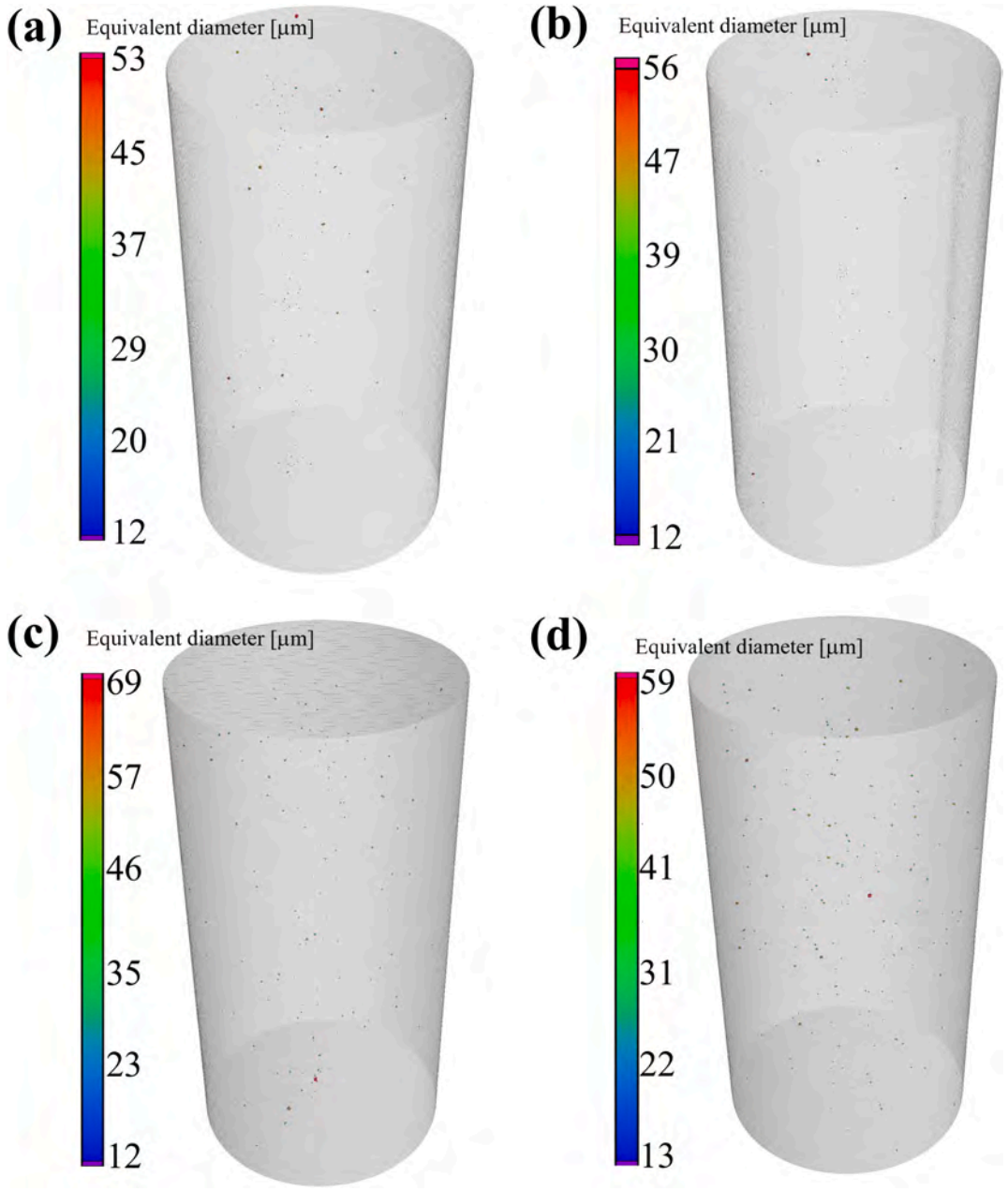

Fig. 6. µ-CT scan results illustrating the internal defect distribution in (a & c) AB and HT (horizontally printed), and (b & d) AB and HT specimens (vertically printed).

The defect counts as a function of the square projected area in the XY plane for LPBF 70/30 Cu–Ni specimens under all processing conditions are presented in Fig. 7. For horizontally printed specimens (Fig. 7a), the AB condition exhibits a dominant pore size in the 10–15µm range. In the HT condition, the peak shifts to larger pores in the 20–25µm range. In addition, the largest defects, exceeding 60µm, appear only in the horizontally printed HT specimen, suggesting localized growth or coalescence of certain pre-existing pores. It is worth noting that for fatigue-sensitive applications, defect size distribution, particularly the presence of the largest pores, plays a more critical role in fatigue life than the small pore size. These large defects in the horizontally printed HT specimens are therefore expected to act as dominant crack-initiation sites and reduce fatigue life, whereas smaller and more uniformly distributed pores may result in a more predictable fatigue response. The effect of defects on fatigue behavior, which reflects a competition between defect-driven and microstructure-driven crack initiation mechanisms, is discussed further in the fractography section. In vertically printed specimens (Fig. 7b), defects in the AB condition are also concentrated in the 10–15µm range. In the HT condition, the pore size is primarily in the 25–30µm range, while the maximum defect remains similar to the AB condition.

Horizontally fabricated specimens typically manifest a higher incidence of volumetric defects, characterized by greater size and numerical density, compared to their vertically fabricated counterparts, even when processed under identical nominal parameters [43,44]. This disparity is fundamentally rooted in the differential thermal dynamics and layer fusion mechanisms inherent to the two build orientations. In the vertical orientation, the relatively small cross-sectional area being processed per layer facilitates a more stable and unidirectional heat flow, which is aligned with the build direction (Z-axis). This thermal stability promotes consistent remelting and effective reheating of previously deposited layers, thereby enhancing inter-layer bonding and melt pool stability.

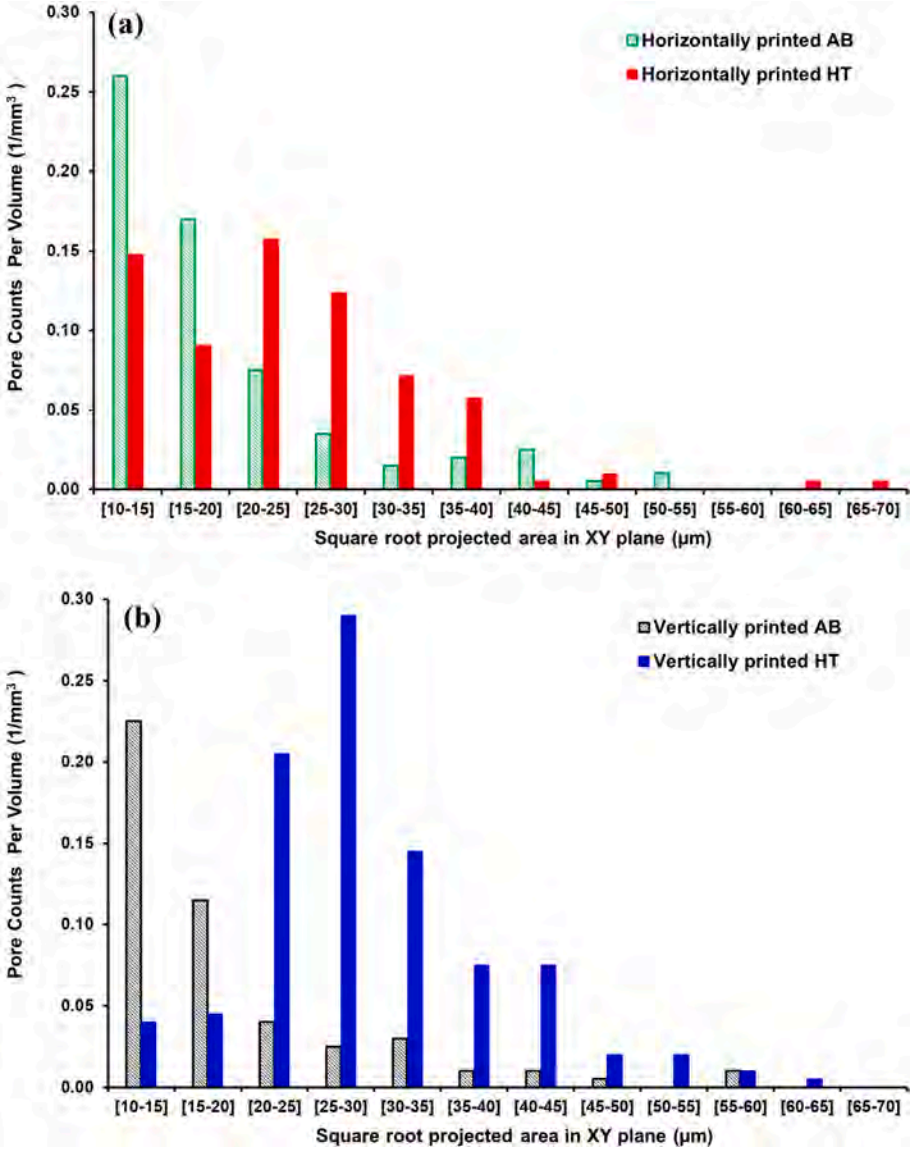

Fig. 7. Defect counts as a function of projected area in XY plan for LPBF 70/30 Cu–Ni specimens; (a) horizontally printed and (b) vertically printed.

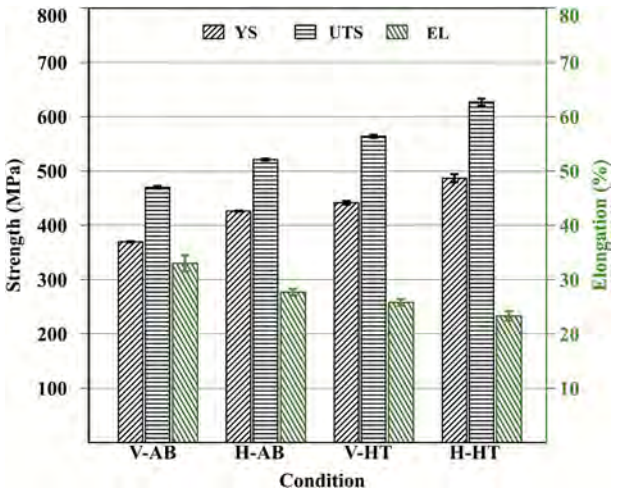

Fig. 8. Columnar charts showing tensile properties of the studied PBF-LB 70/30 Cu–Ni alloy.

The resulting microstructure is generally characterized by lower overall porosity and a reduced prevalence of lack-of-fusion (LoF) defects. Conversely, the horizontal orientation necessitates processing a significantly larger cross-sectional area, which introduces substantial challenges related to thermal management. The resultant uneven heat distribution and elevated thermal gradients across the melt pool can lead to incomplete fusion between adjacent scan tracks. Furthermore, the specific scanning strategy employed in the horizontal plane can induce localized thermal excursions, causing either overheating (leading to keyholing and gas entrapment) or under-melting (exacerbating LoF defects).

3.3. Mechanical properties

Fig. 8 presents the quasi-static uniaxial tensile properties of PBF-LB 70/30 Cu–Ni specimens under various conditions. Horizontally printed specimens, both AB and HT, exhibited higher YS and UTS than their vertically printed counterparts but showed reduced elongation. This difference is primarily due to the alignment of the applied load relative to the melt pool layers. In horizontally printed specimens, the load is parallel to the layers, which reduces sensitivity to interfacial

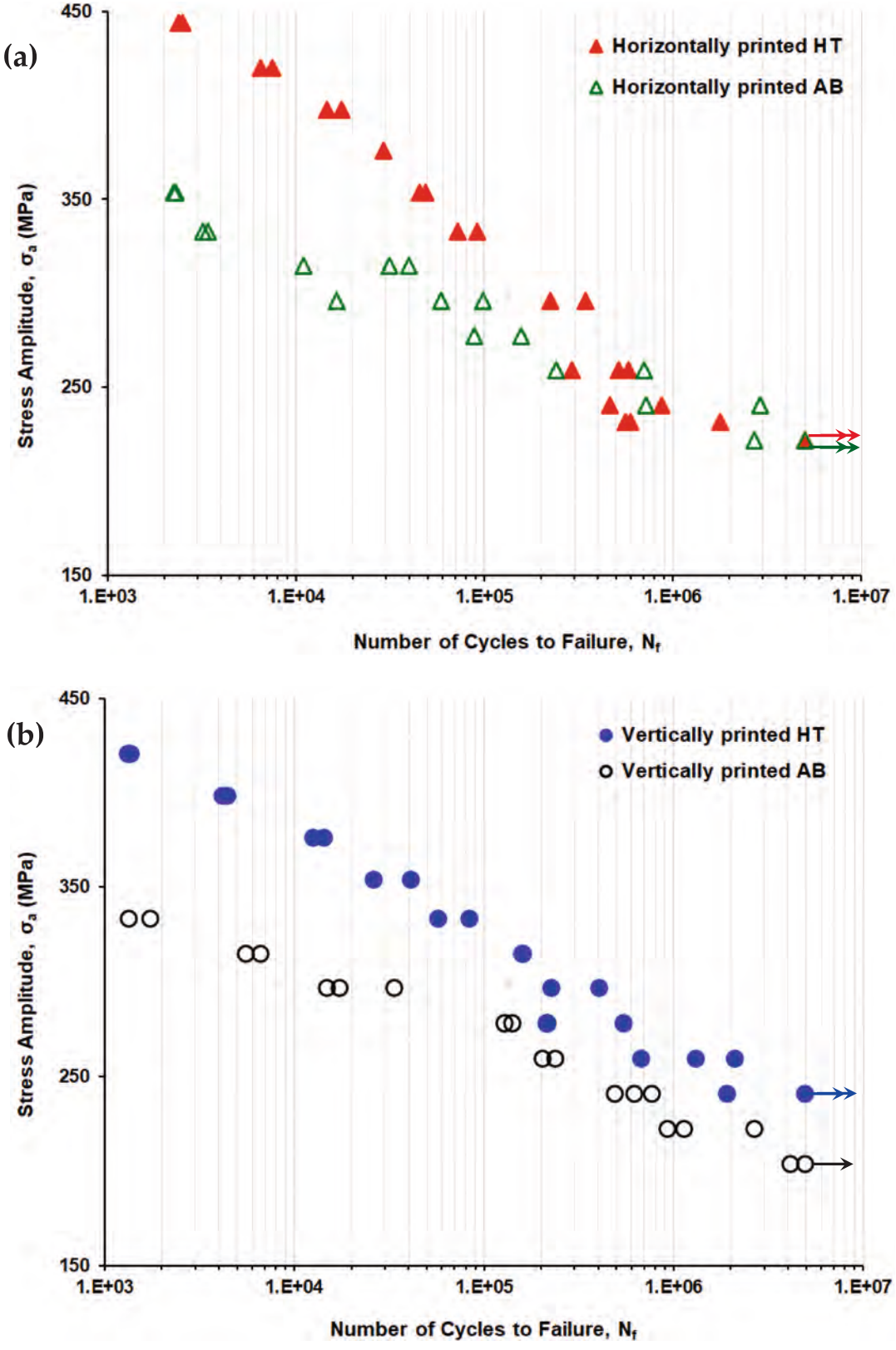

Fig. 9. S-N data of fully-reversed (R = −1) uniaxial fatigue tests; (a) horizontally printed and (b) vertically printed specimens. Arrows indicate runout data.

weaknesses. In contrast, in vertically printed specimens, the load is perpendicular to the additive layer bands, exposing the material to weaker interlayer bonding. As a result, vertically printed specimens generally have lower tensile strength and are more susceptible to failure along the layer interfaces.

The applied post-print HT further enhanced both UTS and YS, primarily through dislocation pinning by solute atoms and potential precipitation of fine Nb-rich particles, along with the formation of more stable dislocation substructures. The strengthening effect of these precipitates has been discussed in detail in the authors' previous work [34].

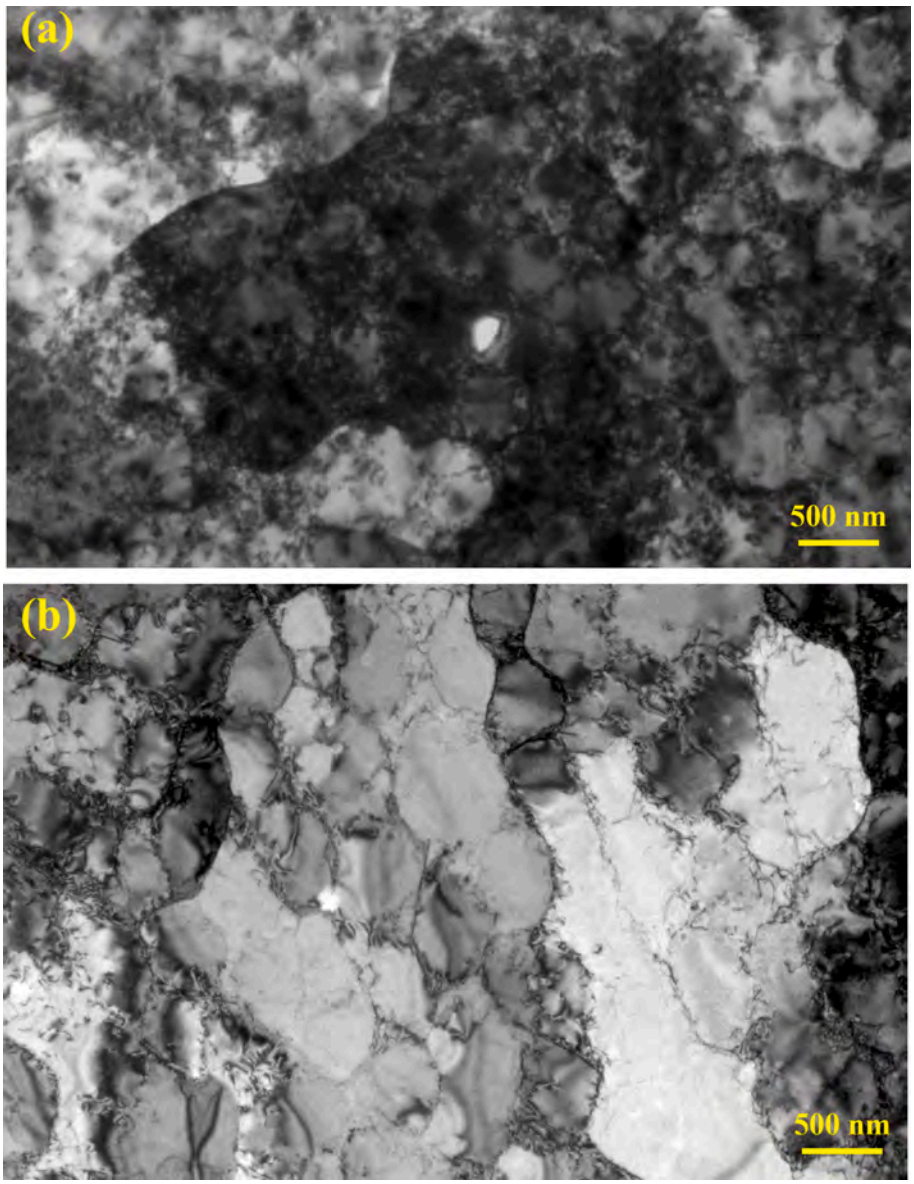

Fig. 10. TEM image of the cells (a) AB state: a large density of less organized dislocations, and (b) HT condition: well-developed cells (subgrains) with dislocation-rich cell boundaries.

Overall, horizontally printed HT specimens achieved the highest strength but the lowest elongation to failure, whereas vertically printed AB specimens demonstrated the lowest strength yet the greatest ductility.

3.4. Fatigue response

3.4.1. S-N data

Fig. 9 shows the fully reversed stress-life (S-N) data for the studied PBF-LB 70/30 Cu–Ni at various conditions (vertically printed AB, horizontally printed AB, vertically printed HT, and horizontally printed HT). The tests were performed at room temperature using a sinusoidal waveform under force-controlled conditions. Specimens that did not fail after 5×10^6 cycles were considered runout specimens, as indicated by arrows in Fig. 9. Since four different conditions were examined, the fatigue data for horizontally printed specimens in both AB and HT states are presented in Fig. 9a, while those for vertically printed are shown in Fig. 9b. This arrangement provides clearer visualization and facilitates direct comparison of the effects of build orientation and HT, thereby reducing potential confusion. In addition, the corresponding fatigue data, including specimens' ID, applied stress levels, number of cycles to failure, and the features observed at the crack initiation sites, are reported in Table S1 (Supplementary Materials). As the primary objective of this study was to investigate the HCF behavior of the alloy, the applied stress levels were chosen to remain within the HCF regime. Tests in the low-cycle fatigue (LCF) regime were not conducted, as they require strain-controlled tests with additional instrumentation such as an extensometer.

We know that the fatigue behavior of AM alloys derives from the complex interaction between AM parameters, AM-induced defect characteristics, microstructural features, and testing conditions, all of which contribute to the inherent scatter observed in fatigue life [45–47]. In this study, experimental conditions and testing procedures were carefully controlled to minimize external influences, allowing the effect of intrinsic material properties and defect characteristics to be isolated as the primary sources of variation. While a certain degree of scatter is inevitable in fatigue data, the fatigue lives of specimens tested at identical stress amplitudes generally remain within the same order of magnitude, indicating acceptable repeatability.

As shown in Fig. 9, during the early stage of the HCF regime ($\sim10^3$

to~10^5 cycles), the fatigue results reflected the material's monotonic tensile behavior. The horizontally printed HT specimens exhibited the highest fatigue life, whereas the vertically printed AB specimens showed the lowest. In this interval, the material response is still dominated by mechanisms governing the quasi-static tensile properties, such as the initial dislocation density (see TEM images in Fig. 10), solid-solution strengthening, and the stability of microstructural features introduced during processing. Consequently, the observed fatigue performance exhibits a strong dependence on the tensile strength and ductility, indicating that the material has not yet entered a regime where pronounced cyclic deformation or damage accumulation governs the fatigue life.

As the stress amplitude decreased, the differences in fatigue performance gradually diminished. Beyond approximately ~10^5 cycles, the horizontally printed specimens, however, exhibited no appreciable sensitivity to HT, with both the HT and AB conditions converging to a comparable fatigue strength of 222MPa. This behavior can be attributed to the defect distribution, particularly the size of the largest defects in the XY plane, which primarily governs fatigue initiation. The vertically printed HT specimens exhibited superior fatigue life compared to the other conditions. The fatigue strength of the vertically printed HT specimen is 241MPa, compared to 204MPa for the vertically printed AB specimen.

The fatigue performance of the HT specimens is superior to that of the AB specimens, particularly at higher stress amplitudes. This improvement arises from the combined effects of stress relief and higher strength (e.g., precipitation hardening) of the HT specimens relative to AB materials [34]. In the AB condition, PBF-LB specimens inherently retain substantial residual stresses arising from the steep thermal gradients and rapid localized heating–cooling cycles characteristic of the process. These tensile residual stresses act as an additional driving force for fatigue damage, promoting earlier crack initiation and facilitating faster crack propagation, thereby detrimentally affecting the overall fatigue performance. Post-processing HT, however, effectively relieves these residual stresses, thereby lowering the effective local stress intensity at potential crack-initiation sites. This stress relaxation mitigates the likelihood of early crack nucleation and slows subsequent crack growth, contributing to the improved fatigue performance observed in HT specimens. Additionally, as detailed in our previous work [34], HT leads to the formation of fine niobium-rich precipitates, which impede dislocation motion and thereby increase the strength and toughness of the material.

In horizontally printed specimens (Fig. 9a), at $N_f > 2\times10^5$ cycles, the disparity in fatigue performance between the HT and AB conditions progressively diminished. Such convergence indicates a shift in the dominant fatigue mechanism. At longer lives, where the applied stress amplitudes are lower, global (bulk) strength metrics (such as YS, UTS, and even bulk hardness) lose much of their controlling contribution to fatigue life. Instead, fatigue performance becomes increasingly governed by microstructure-sensitive, defect-controlled crack-initiation processes, in which failure is dictated by the locally stressed regions. In this regime, the controlling factor is no longer the average material strength, but rather whether the material contains critically weak local features capable of triggering crack initiation. These features may include process-induced volumetric defects (e.g., pores and LoF defects) and/or crystallographic facets favorably oriented towards early microcrack formation.

Although HT improves bulk mechanical properties (e.g., YS and UTS), it does not necessarily remove such microscopic stress concentrators (e.g., volumetric defects and facets). Consequently, as fatigue crack initiation becomes dominated by stochastic, localized mechanisms at low stress amplitudes, the deterministic benefits of HT become less pronounced. This behavior is consistent with the observed convergence in fatigue data, where some as-built specimens exhibit fatigue lives comparable to, or even exceeding, those of their heat-treated counterparts. Importantly, XCT indicates that HT does not reduce the defect size or defect population; in some cases, the largest defects are comparable to, or slightly larger than, those in the AB condition. Therefore, the observed improvement in fatigue performance after HT cannot be attributed to defect mitigation, but instead to microstructural evolution and dislocation-level rearrangement. The dislocation structure and its evolution with HT are other key factors in controlling fatigue life between HT and AB conditions. The TEM images in Fig. 10 reveal pronounced differences in dislocation structures between the AB (Fig. 10a) and HT (Fig. 10b) conditions. In the AB state, dense dislocation tangles are concentrated within the grains and along cellular boundaries (Fig. 10a). The rapid solidification and steep thermal gradients characteristic of the PBF-LB process generate substantial thermal stresses that may exceed the local yield strength, thereby promoting extensive dislocation formation. These dislocations accumulate as tangled networks or dislocation forests, producing high internal strain energy and a highly disordered dislocation arrangement.

Following post-fabrication HT, significant dynamic recovery occurs. Enhanced dislocation mobility facilitates rearrangement, annihilation, and reorganization into lower-energy configurations. As a result, the dislocation network becomes more ordered, dislocations segregate into well-defined cell walls or dislocation-rich boundaries, while the interiors of the cells become comparatively depleted of dislocations (Fig. 10b). This reconfiguration reduces the overall dislocation density and internal strain energy, yielding a more stable and partially recovered microstructure. The contrast between Fig. 10a & b demonstrates the transition from a highly entangled dislocation network to a more organized dislocation-cell morphology. This reconfiguration delays crack initiation, improving early-stage fatigue performance. In horizontally printed specimens, however, the recovered dislocation walls intersect the loading direction in ways that initially resist slip but generate localized stress concentrations, accelerating persistent slip band (PSB) formation and microcrack coalescence as cycling progresses. Vertically printed specimens benefit from more favorable dislocation alignment along the load axis, delaying PSBs and stabilizing early crack propagation paths, which sustains higher fatigue resistance into the mid-to-late HCF regime.

Phase evolution and nanoscale precipitate/oxide formation during HT further modulate fatigue behavior. In the AB state, rapid cooling suppresses precipitation, yielding a nearly single-phase α-Cu matrix with trace nanoscale features. Post-HT, Nb-rich secondary phases such as $FeNb_4S_8$, $NbFeO_4$, and $NbNi_3$ nucleate in small volume fractions (~0.2–0.5%), providing localized precipitation strengthening that enhances early fatigue resistance. Simultaneously, SiO_2 content increases from~0.43% to~0.71%, introducing brittle regions that act as preferential crack nucleation sites [34]. The strengthening from Nb-rich phases improves resistance to initial plasticity, but the heterogeneous distribution of brittle oxides (e.g., SiO_2) and inclusions creates localized stress concentration (localized brittleness) that accelerates facet-induced crack initiation and microstructurally small crack propagation.

The Basquin equation is presented in Fig. S2 (Supplementary Materials), where the fitting was carefully performed by excluding S-N data outside the HCF regime to ensure accuracy. Data points below 10^3 cycles were removed for analysis, as they are within the LCF regime and are governed by different deformation mechanisms. Likewise, run-out specimens that did not fail within 5×10^6 cycles were excluded. The Basquin equation takes the form $\sigma_a = aN_f^b$, where σ_a represents the stress amplitude, a is the fatigue strength coefficient, N_f denotes the number of cycles to failure, and b is the fatigue strength exponent.

Analysis of the Basquin fits for all conditions reveals distinct trends. For the AB specimens, both horizontal (horizontally printed AB) and vertical (vertically printed AB) conditions exhibit nearly parallel fatigue curves, with very close fatigue strength exponents (−0.057 and −0.060, respectively). This indicates similar fatigue mechanisms, with only minor differences in interceptive values (546 for horizontally printed AB and 532 for vertically printed AB). In contrast, the HT specimens show

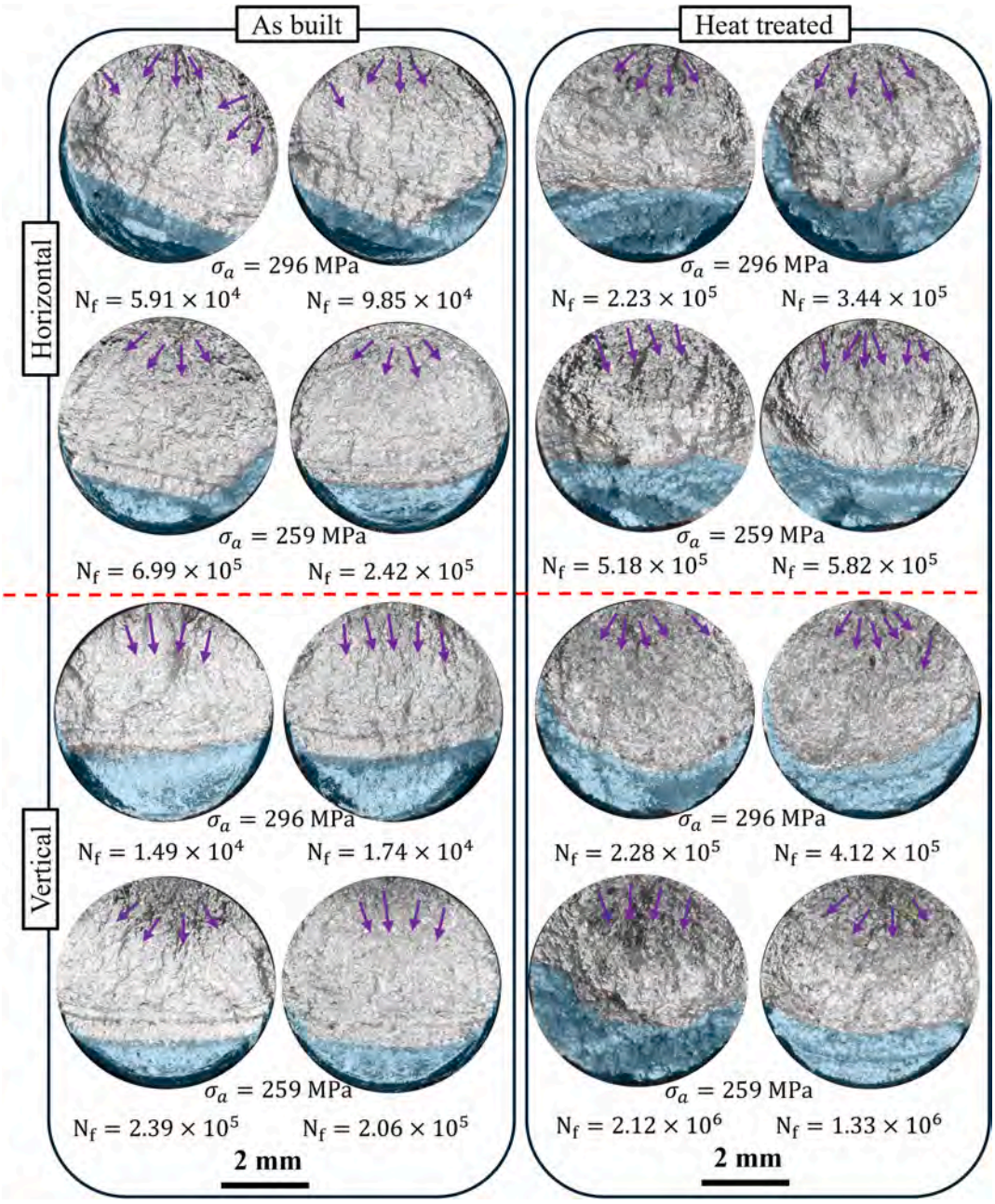

Fig. 11. Fatigue fractured surface of the 70/30 Cu–Ni specimens at σ_a=259MPa and 296MPa for different conditions.

more pronounced differences. The interceptive values are considerably higher (~1156 for horizontally printed HT and ~749 for vertically printed HT), consistent with the improved tensile strength observed after HT. The fatigue strength coefficient (σ_f') increased significantly following HT in both orientations, confirming that thermal processing enhanced fatigue resistance by relieving residual stresses and promoting precipitation strengthening.

More importantly, the fatigue strength exponents diverge significantly: −0.114 for horizontally printed HT and−0.075 for vertically printed HT. This difference in slope indicates that while horizontally printed HT specimens initially demonstrate higher fatigue strength, the steeper slope results in a faster decline with decreasing stress amplitude. Furthermore, the more negative fatigue strength exponent (b) observed after HT suggests a steeper decline in fatigue life with increasing stress amplitude, reflecting the higher strength but slightly reduced ductility of the HT material. Overall, these Basquin parameters quantitatively capture the improvement in fatigue behavior induced by HT and the persistent orientation-dependent anisotropy characteristic of PBF-LB alloys. Additionally, the coefficient of determination (R^2) values obtained from the Basquin fits were 0.93 and 0.95 for horizontally printed AB and HT specimens, respectively, and 0.96 for both vertically printed conditions. The slightly higher R^2 values observed for the vertically printed specimens suggest that their fatigue behavior follows a more consistent trend.

To model the experimental scatter, the probabilistic S-N curves (P-S-N) have been estimated. Several models can be considered to fit the experimental data, and to verify a possible asymptotic trend (i.e., a fatigue limit) above 10^6 cycles. However, even if runout data have been experimentally found, they are close to experimental failures, thus not suggesting an asymptotic trend. The assumption of a fatigue limit would be a risky non-conservative extrapolation, not supported by experimental evidence. Accordingly, the experimental data have been fitted

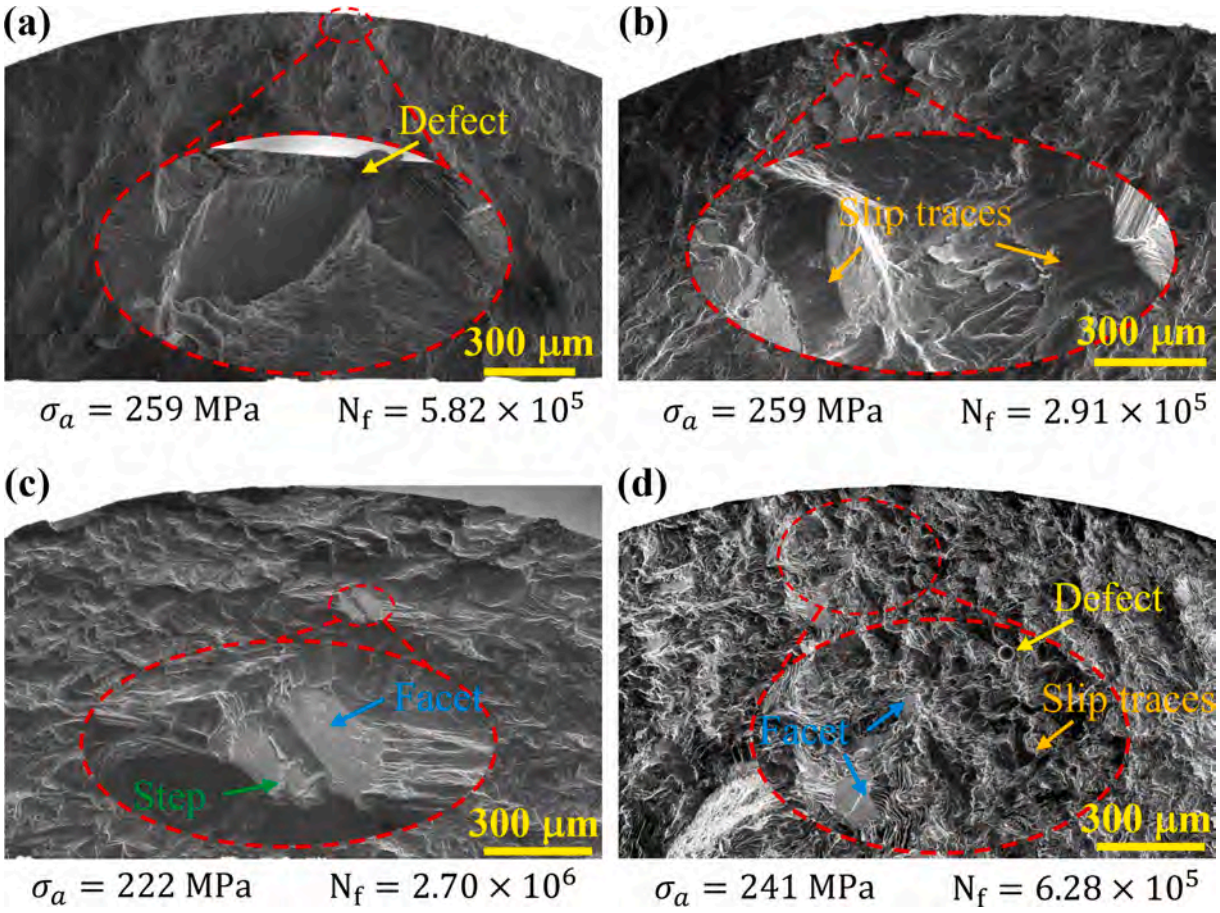

Fig. 12. SEM images of fatigue fracture surfaces illustrating different crack-initiation mechanisms: (a) initiation at a surface defect (horizontally printed HT condision), (b) slip traces within the crack-initiation region (horizontally printed HT condition), (c) initiation on a crystallographic facet (horizontally printed AB condition), and (d) combined facet- and defect-assisted initiation (vertically printed AB condition).

with a linear model in a log–log plot, by assuming that the fatigue life, i.e., the random variable $Y = \log_{10}(N_f)$, where N_f is the number of cycles to failure follows a Normal distribution. In this model, the mean value of Y is linearly correlated with the logarithm of the applied stress amplitude (σ_a).

Furthermore, the standard deviation is considered invariant throughout the entire life range examined. The cumulative distribution function (*cdf*) of the fatigue life $F_{Y|s_a}$ can therefore be expressed as $F_{Y|s_a} = \Phi\left(\frac{y-(a_Y \bullet \log_{10}(s_a)+b_Y)}{\sigma_Y}\right)$, being $\Phi(\bullet)$ the *cdf* of a standardized normal distribution. The coefficients a_Y and b_Y, describing the linear variation of the fatigue life with respect to the applied stress amplitude, and the standard deviation, are to be estimated from the experimental data. In particular, the estimation process has been carried out by applying the Maximum Likelihood Principle to concurrently consider failures and runout data. Given the constant coefficients, the α-th quantile P-S-N curve can be estimated by replacing $F_{Y|s_a}$ with α, and by solving the $F_{Y|s_a}$ equation with respect to s_a for the range of N_f of interest. Fig. S3 (Supplementary Materials) plots the estimated P-S-N curves (10-th, 50-th, and 90-th) for the investigated conditions: Fig. S3(a) for the horizontally printed and Fig. S3(b) for the vertically built specimens.

The P-S-N curves in Fig. S3 (Supplementary Materials) agree with the experimental data, with, for each experimental condition investigated, more than 75% of the experimental failures within the 10-th and 90-th quantile P-S-N curves. For the horizontally printed specimens, the P-S-N curves for the HT and AB specimens overlap from 10^5 cycles, thus confirming the results of the previous analysis in a statistical framework, i.e., that HT specimens have better fatigue performances at high applied stress amplitude and a limited number of cycles. Within the 10^5 cycles and 10^6 cycles, there is no statistical difference. On the other hand, above 10^6 cycles, AB specimens show a higher fatigue strength, with the P-S-N curves that stop overlapping at 5×10^6 cycles. This trend for a larger number of cycles, beyond those investigated in the present paper, should be verified experimentally to avoid risky non-conservative extrapolations. For the vertically printed specimens, the P-S-N curves do not overlap for the life range investigated, signifying that the fatigue response is statistically significantly different, with the HT being effective in improving the fatigue response.

3.4.2. *Post-mortem characterization (fractography)*

An initial overview of representative fracture surfaces is provided by the optical micrographs in Fig. 11, showing specimens tested at stress amplitudes of 259MPa and 296MPa. The images include both AB and HT conditions for vertically and horizontally printed specimens. These images were selected to illustrate typical fatigue crack initiation behavior, which was systematically observed across all tested specimens. Fatigue cracks were consistently observed to initiate either at the specimen surface or within subsurface regions.

To further explain the fatigue fracture mechanisms in the studied PBF-LB 70/30 Cu–Ni alloy, representative high magnification SEM images from various specimen conditions are presented in Fig. 12. These micrographs provide a detailed overview of the distinct initiation modes observed. While a universal conclusion cannot be drawn for all conditions, a clear trend emerges linking the initiation mechanism to the presence and size of surface defects.

A systematic analysis indicates that, while surface defects can

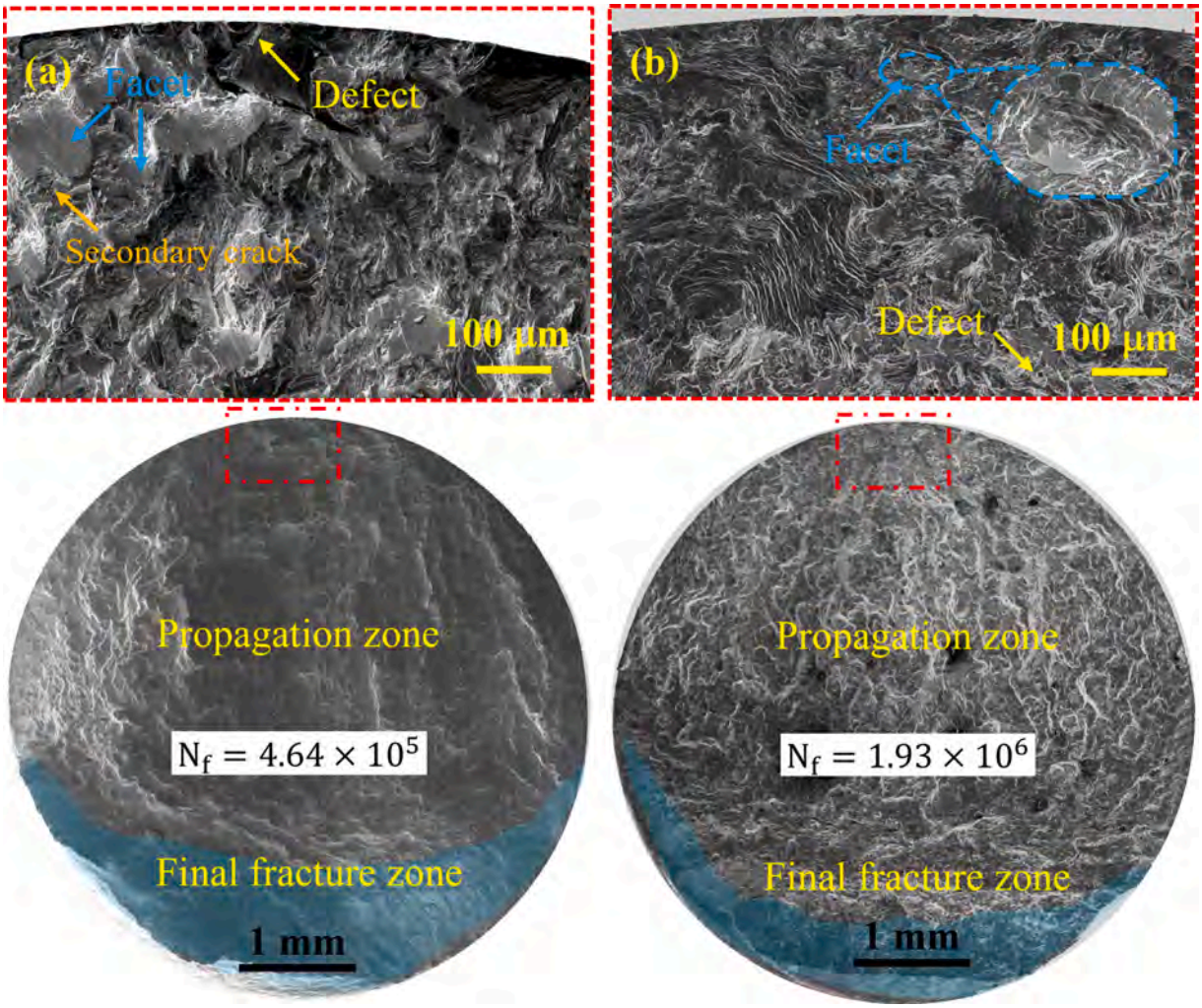

Fig. 13. SEM image of the fatigue fractured surface; (a) horizontally printed HT F21 (σ_a=241MPa & N_f=4.64×10^5 cycles), and (b) vertically printed HT F22 (σ_a=241MPa & N_f=1.93×10^6 cycles).

contribute to crack initiation, crystallographic facet features were more frequently involved. Three primary initiation modes were identified: (*i*) direct initiation from relatively large surface process-induced defects (Fig. 12a), such as sub-surface LoF; (*ii*) initiation on a prominent surface and subsurface crystallographic facet (Fig. 12b & c), which occurred more commonly; and (*iii*) facet-assisted initiation (Fig. 12d) in which a nearby defect (e.g., fine gas porosities) appeared to act as a secondary trigger, consistent with a localized brittle-like fracture mechanism. Based on the data summarized in Table S1 (Supplementary Materials), 13 out of 78 specimens exhibited defect-controlled initiation (Group *i*), 51 out of 78 specimens showed initiation solely from crystallographic facets (Group *ii*), and 14 out of 78 specimens exhibited combined facet and defect-assisted initiation within the crack initiation zone (Group *iii*). In most cases, specimens exhibiting defect-initiated crack initiation showed shorter fatigue lives than those governed by facet-controlled or facet/defect-assisted mechanisms. Consequently, a significant portion of the scatter in the fatigue data arises from the presence of defects and the associated differences in crack-initiation behavior.

In Fig. 12b, slip traces are visible on the facet surface, indicating that failure was governed by cyclic slip within a single grain. These features confirm microstructure-controlled, shear-mode crack growth characteristic of Stage I crack propagation in the HCF domain. In Fig. 12c, higher-magnification imaging reveals step-like features on the facets. These steps form when the advancing crack encounters local obstacles or stress variations and shifts onto a nearby, nearly parallel slip plane. They therefore mark the boundaries where the crack front transitions between crystallographic planes.

The presence of PBF-LB-induced volumetric defects locally elevates stress amplitude, where the microstructure is more prone to fracture rather than slip. Brittle-like crack initiation at a facet indicates that, despite the overall ductile behavior of the bulk material, the local microstructure in that region is brittle with reduced toughness, often due to unfavorable crystallographic orientation, segregation of alloying elements, or other microstructural heterogeneities inherent to the PBF-LB process. In such areas, the applied cyclic stresses were sufficient to trigger brittle events along specific crystallographic planes, which then acted as microcrack initiation sites. Once formed, these facets facilitated further crack propagation under cyclic loading, ultimately leading to fatigue failure.

Examination of fracture surfaces from both horizontally and vertically printed specimens, in the AB and HT conditions, reveals that faceted features frequently coexist with process-induced volumetric defects. This observation indicates that, in the studied PBF-LB 70/30 Cu–Ni alloy, fatigue crack initiation is strongly influenced by locally brittle microstructural mechanisms associated with crystallographic faceting, rather than being governed solely by AM-induced gas porosity and/or LoF defects. When large surface-connected defects are present, they tend to dominate crack initiation. However, crystallographic facets are also observed in specimens where defects are small or not directly involved in initiation, which shows that intrinsic microstructural factors

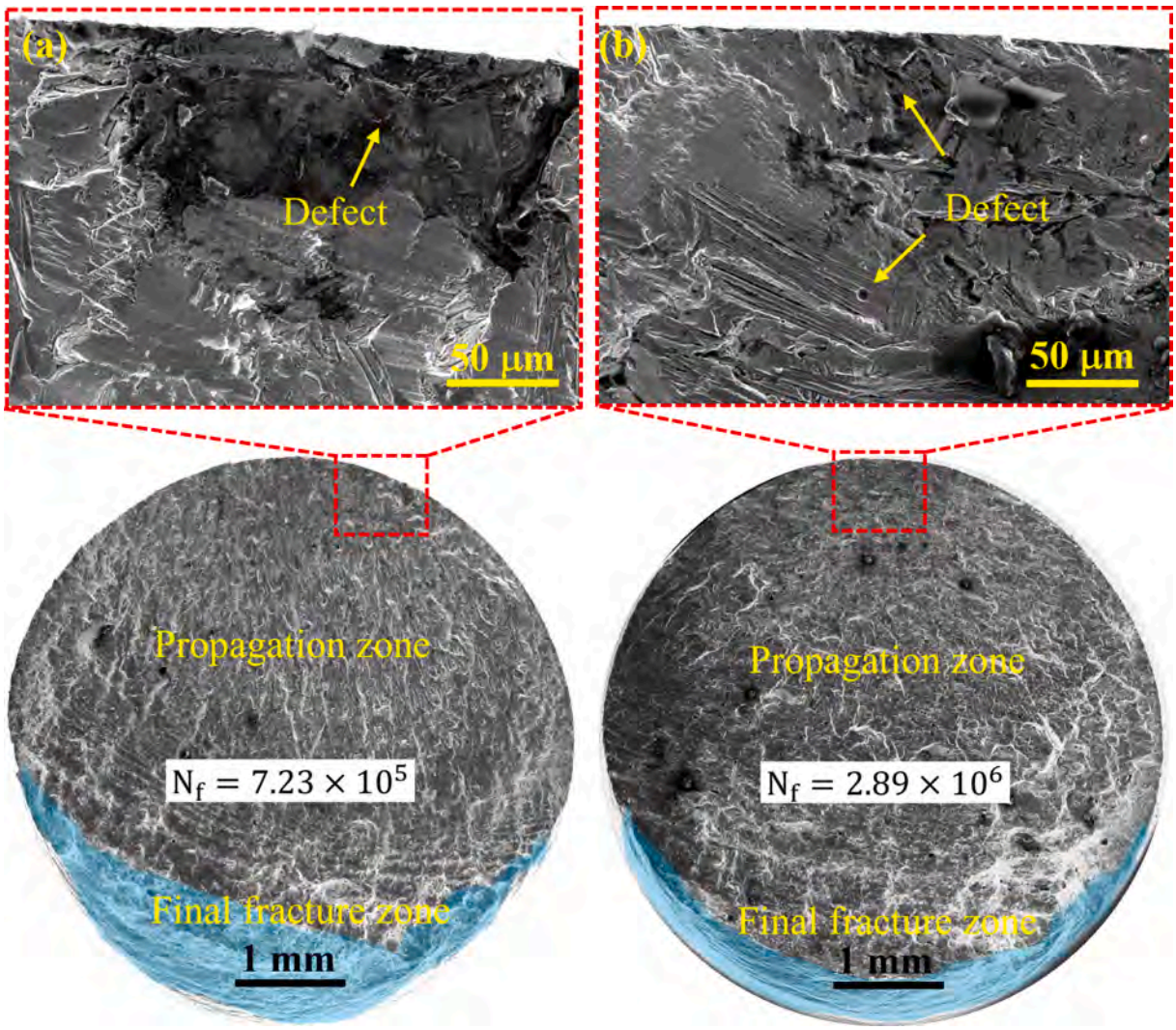

Fig. 14. SEM image of the fatigue fractured surface of the studied 70/30 Cu–Ni at σ_a=241MPa for horizontally printed AB specimens; (a) F15 (σ_a=241MPa & N_f=7.23×10^5 cycles), and (b) F18 (σ_a=241MPa & N_f=2.89×10^6 cycles).

consistently contribute across processing and orientation conditions. For a ductile, single-phase alloy such as cupronickel, one would typically expect a non-crystallographic, striated fracture surface. The emergence of facets is more characteristic of near-threshold fatigue or of high-strength, complex alloys. For example, nickel-based superalloys such as Inconel 718 often exhibit pronounced crystallographic fracture due to their planar slip behavior [48,49]. In FCC crystals, plastic deformation occurs primarily by dislocation motion along the {111}⟨110⟩ slip system, which represents the most closely packed planes and directions [50–52]. Materials exhibiting planar slip, such as certain FCC superalloys, tend to localize plastic deformation on discrete planes, promoting facet formation. The fatigue crack nucleates from these large crystallographic facets and subsequently propagates until final fracture. Observing similar features in 70/30 Cu–Ni, therefore, suggests a departure from its expected ductile fatigue failure mode.

Fig. 13 presents a comparison of the fracture surfaces of horizontally and vertically printed HT specimens, both tested at a constant stress amplitude of 241MPa, to investigate the significant discrepancy in their fatigue lives. The horizontally printed specimen (Fig. 13a) displays several features indicative of a faster failure (4.64×10^5 cycles). A defect attached to the surface, along with several sub-surface large facets, is visible, serving as the primary initiation site and a stress concentrator. Furthermore, the fracture surface exhibits evidence of secondary cracking in the propagation area. This combination of a dominant initiating flaw and multiple sites for crack nucleation contributed to its reduced fatigue life. In contrast, the vertically printed specimen (Fig. 13b), which endured a significantly greater number of cycles (1.93×10^6 cycles), shows a more refined fracture surface. Both the observable defects and the crystallographic facets are visibly smaller, sub-surface, and less pronounced than in their horizontally printed counterpart. This reduction in the size of critical initiating features and the sub-surface location of such fine facets is directly responsible for the vertically printed specimen's enhanced resistance to fatigue crack initiation and its correspondingly superior fatigue performance.

Fig. 14 presents the fracture surfaces of two horizontally printed AB specimens tested at a stress amplitude of 241MPa, which exhibited a significant disparity in fatigue life. In both cases, crack initiation occurred at the specimen surface. Notably, only limited evidence of crystallographic faceting was observed at the crack origin, suggesting a defect-controlled or predominantly non-crystallographic initiation mechanism. The cause for the large scatter in fatigue life becomes evident upon detailed examination of the initiation sites. Fig. 14a reveals that the shorter-life specimen failed due to a large surface-breaking defect, which acted as a stress concentrator and greatly accelerated crack initiation. In contrast, the fracture surface of the longer-life specimen, shown in Fig. 14b, contains a much smaller surface defect. This smaller flaw required a substantially greater number of cycles to activate, which explains the significantly longer fatigue life.

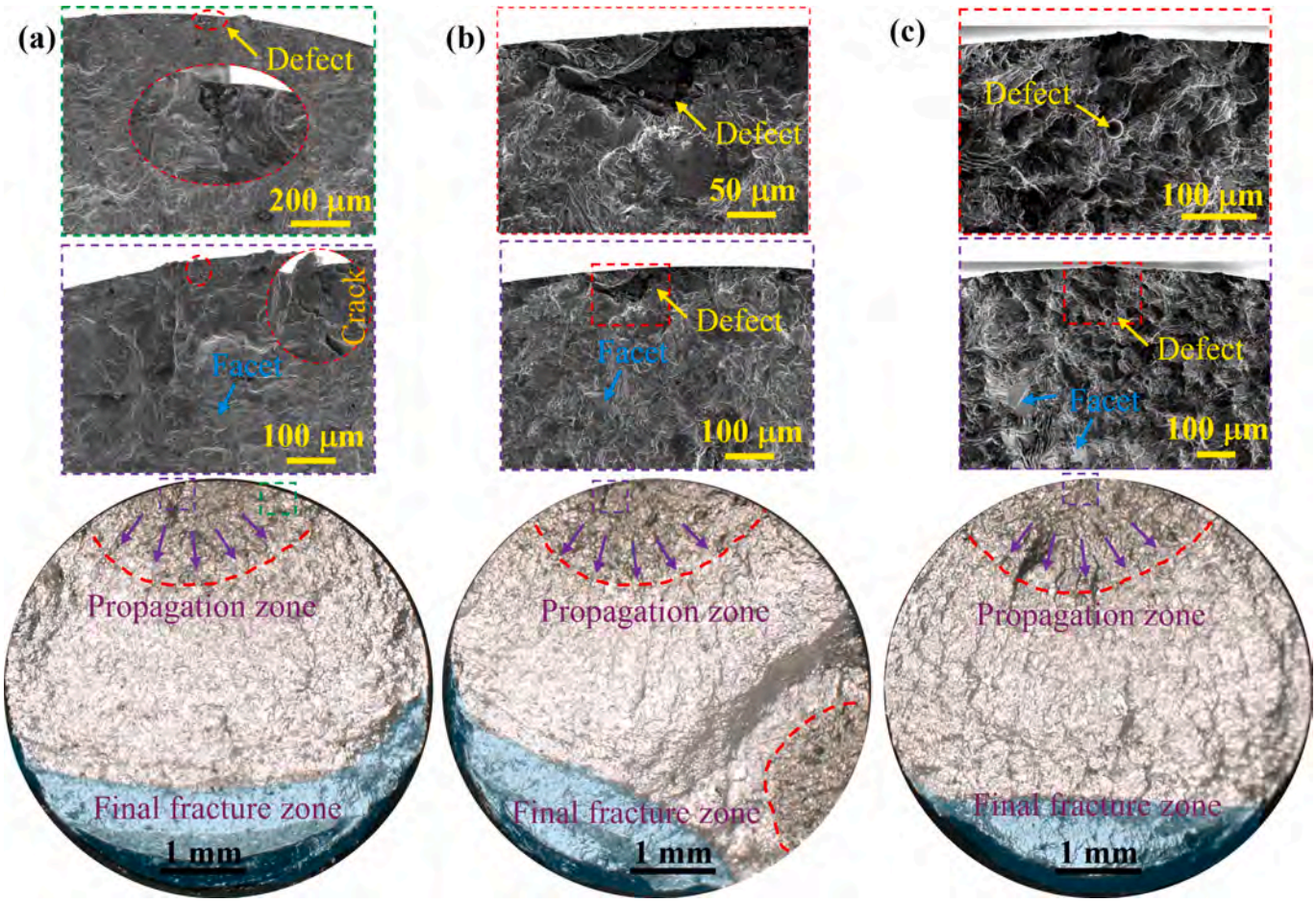

Fig. 15. Optical and SEM images of vertically printed specimens in AB condition; (a) F7 (σ_a=241MPa & N_f=7.74×10^5 cycles), (b) F8 (σ_a=241MPa & N_f=4.93×10^5 cycles), and (c) F20 (σ_a=241MPa & N_f=6.28×10^5 cycles).

Fig. 15 presents optical and SEM images of the fatigue fracture surfaces for vertically printed specimens in the AB condition; all tested at a stress amplitude of 241MPa. The full optical images show a distinct dark region highlighted with a dashed red line, corresponding to the crack initiation zone. In addition, the final fracture region is indicated in Fig. 15 using a blue shadow.

In Fig. 15a (specimen F7), which exhibited a fatigue life of 7.74×10^5 cycles, the crack initiated from two sites. High-magnification SEM imaging of the first site (purple box) reveals a pronounced crystallographic facet. A separate surface-initiated crack is also observed. At the second site (green box), a small surface defect is present; although it assisted crack initiation, it does not appear to have been the primary initiation location. In Fig. 15b (specimen F8), the optical image shows two initiation sites in different locations; however, SEM examination of the principal initiation region reveals a large surface defect. The presence of this large defect significantly accelerated crack initiation and explains the lower fatigue life observed for this specimen. In Fig. 15c (specimen F20), the crack initiated from a single site and propagated to the final

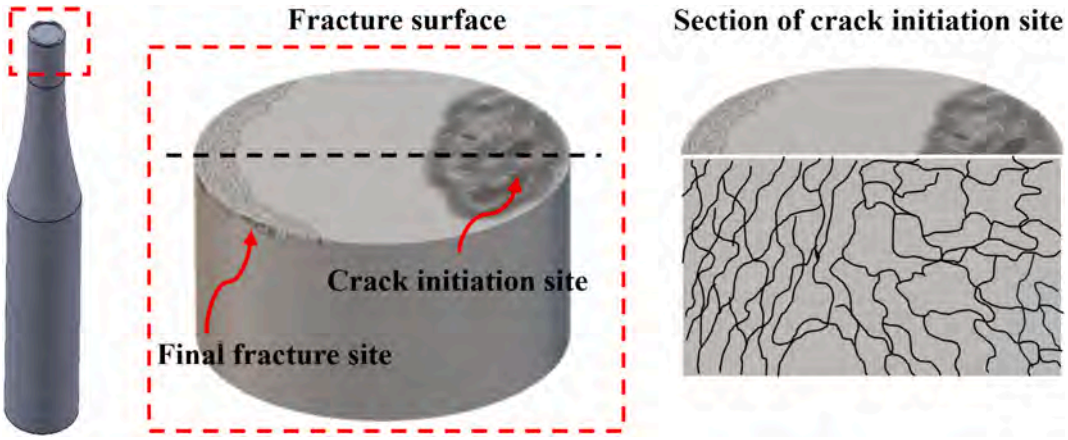

Fig. 16. Schematic of the fracture surface and the post-fatigue EBSD procedure near the crack initiation region on the vertical cross-section of the fractured specimens.

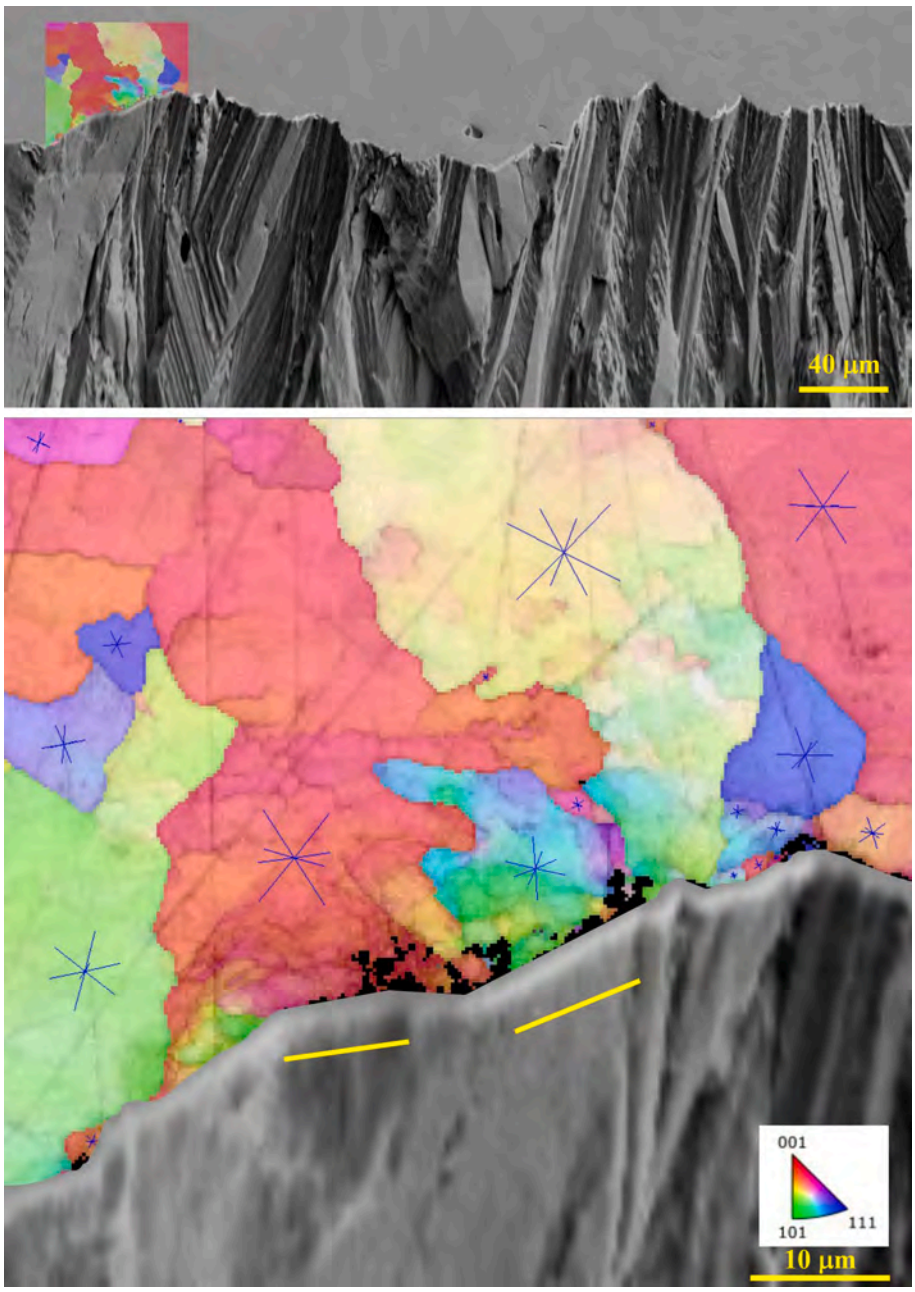

Fig. 17. Post-fatigue EBSD analysis (BC + IPF maps) near the crack initiation region for the AB horizontally printed specimen (F14: σ_a=222MPa & N_f=2.27×10^6 cycles).

fracture. The high-magnification SEM image shows several facets within the initiation region, along with a small gas pore that does not appear to have substantially influenced fatigue life.

Overall, specimens F7 and F20 (Fig. 15a & c) exhibit similar fatigue lives and comparable fracture-surface features. In contrast, the presence of a large surface defect in specimen F8 (Fig. 15b) led to a pronounced reduction in fatigue life, underscoring the critical role of defect size in crack initiation under cyclic loading.

Given the facet-rich fracture surfaces, it appears that although defect-driven initiation occurs in some specimens, the stress concentrations associated with PBF-LB-induced volumetric defects, such as gas porosity and LoF defects, were, in most cases, not sufficient to control the overall failure process. This interpretation is supported by the absence of the fisheye patterns and the fine-grained area (FGA) that are typically observed around volumetric defects in many AM alloys and are characteristic of defect-mediated crack initiation in the HCF regime. The lack of these signatures indicates that, even when defects are present, crack initiation in PBF LB 70/30 Cu–Ni is most often governed by microstructural factors (i.e., facts induced by local brittleness). Indeed, when fine gas porosity defects are present within the maximum-stress region (e.g., Fig. 15c), fatigue crack initiation predominantly occurs from the faceted grain(s). That is, when the characteristic size of porosity is smaller than that of the relevant microstructural heterogeneities, crack initiation may be governed by microstructural features rather than porosity defects. This can be interpreted as a case of competition between defect-driven and microstructure-driven crack initiation, where the alloy's intrinsic microstructural features, rather than pre-existing AM-induced interior defects, act as the primary life-limiting factor in various AM alloys. This, in turn, challenges conventional approaches to assessing fatigue performance that rely primarily on interior volumetric defects (e.g., porosity and/or LoF) metrics. Such competition has been stated by Wu et al. in rotating bending fatigue of

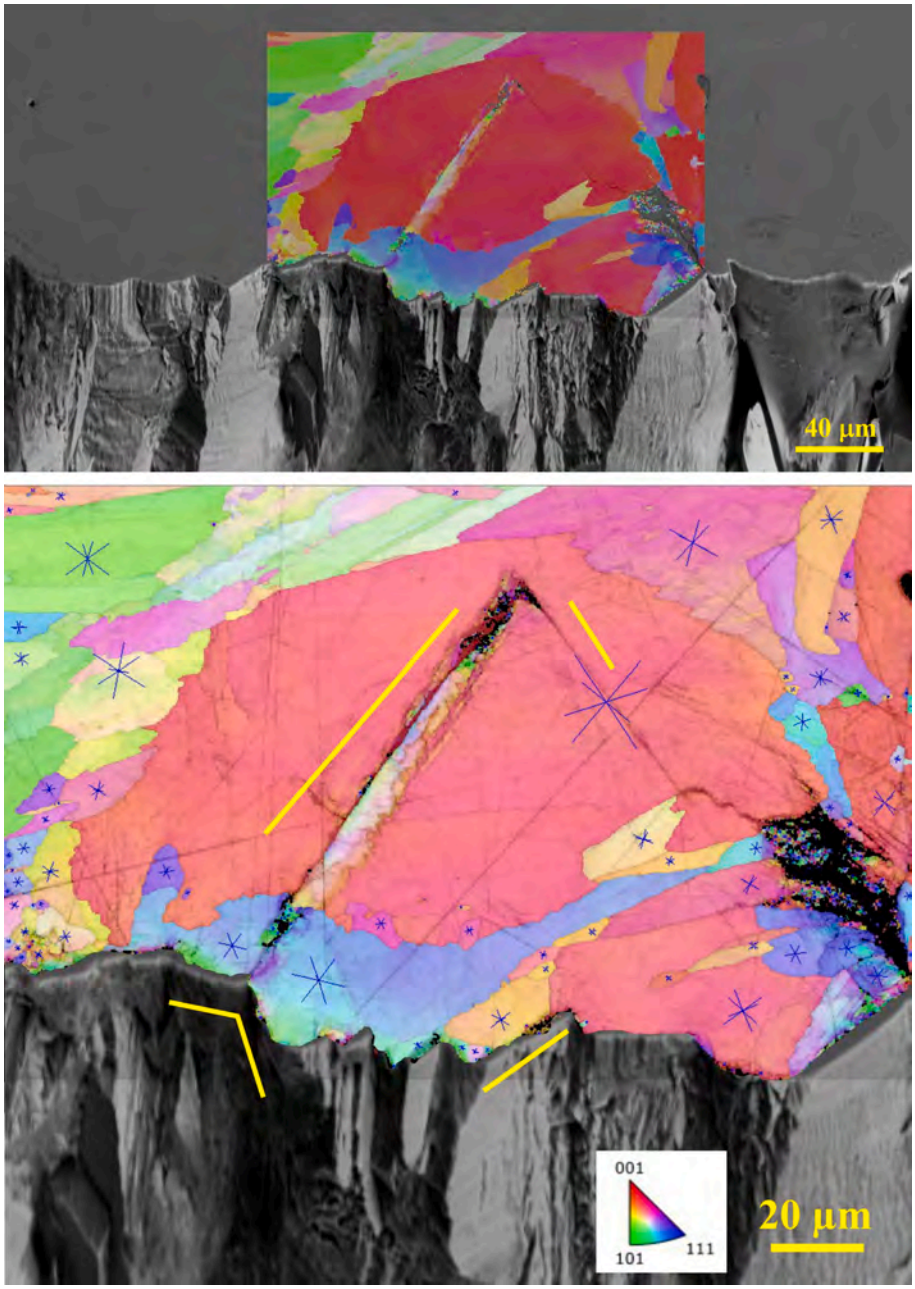

Fig. 18. Post-fatigue EBSD analysis (BC + IPF maps) near the crack initiation region for horizontally printed HT specimen (F21: σ_a=241MPa & N_f=4.64×10^5 cycles).

AM Ti-6Al-4V [53] and Nandi et al. in uniaxial fatigue of AM Inconel 718 [54].

To clarify the local microstructural conditions beneath the crack origin, we examined the EBSD data obtained from sections cut directly below the initiation site and oriented perpendicular to the fracture surface (Fig. 16). These analyses were performed for both the AB (Fig. 17) and HT (Fig. 18) specimens. The direct slip trace analysis is impossible to perform on post-mortem polished samples. Therefore, band contrast (BC) and IPF maps of the AB and HT specimens were generated, onto which theoretical traces of the {111} planes were plotted on the grain structure. In both AB and HT conditions (Figs. 17 and 18), the IPF contrast shows that the subsurface region surrounding the faceted initiation area is dominated by a limited set of crystallographic orientations, suggesting a strong localization of strain within grains favorably aligned for the activation of the primary {111}<110> slip systems. Most of the facets observed on the fracture cross-section correspond to these crystallographic planes, indicating that crack initiation proceeded through cyclic dislocation accumulation on the {111} planes (marked by yellow lines). Fig. 17 presents a localized crack through the {111} plane in the green–blue grain in the map center. Moreover, a significant dislocation accumulation near the crack surface was confirmed by the geometrically necessary dislocations (GNDs) analysis (Fig. 19a).

In the HT specimen (Fig. 18), the precise alignment of an internal crack segment, which propagates entirely within a single grain, with the calculated trace of a {111} crystallographic plane provides direct evidence of the governing failure mechanism. This alignment indicates that crack initiation and early-stage crystallographic propagation are driven by intense strain localization along the highly stressed {111}<110> primary slip system, consistent with the well-established fatigue behavior of FCC alloys. The GND analysis (Fig. 19b) revealed a shallower accumulation depth of dislocations near the crack edges, which is attributed to the pre-existing distinct dislocation patterns.

Fig. S4 (Supplementary Materials) displays the typical morphology

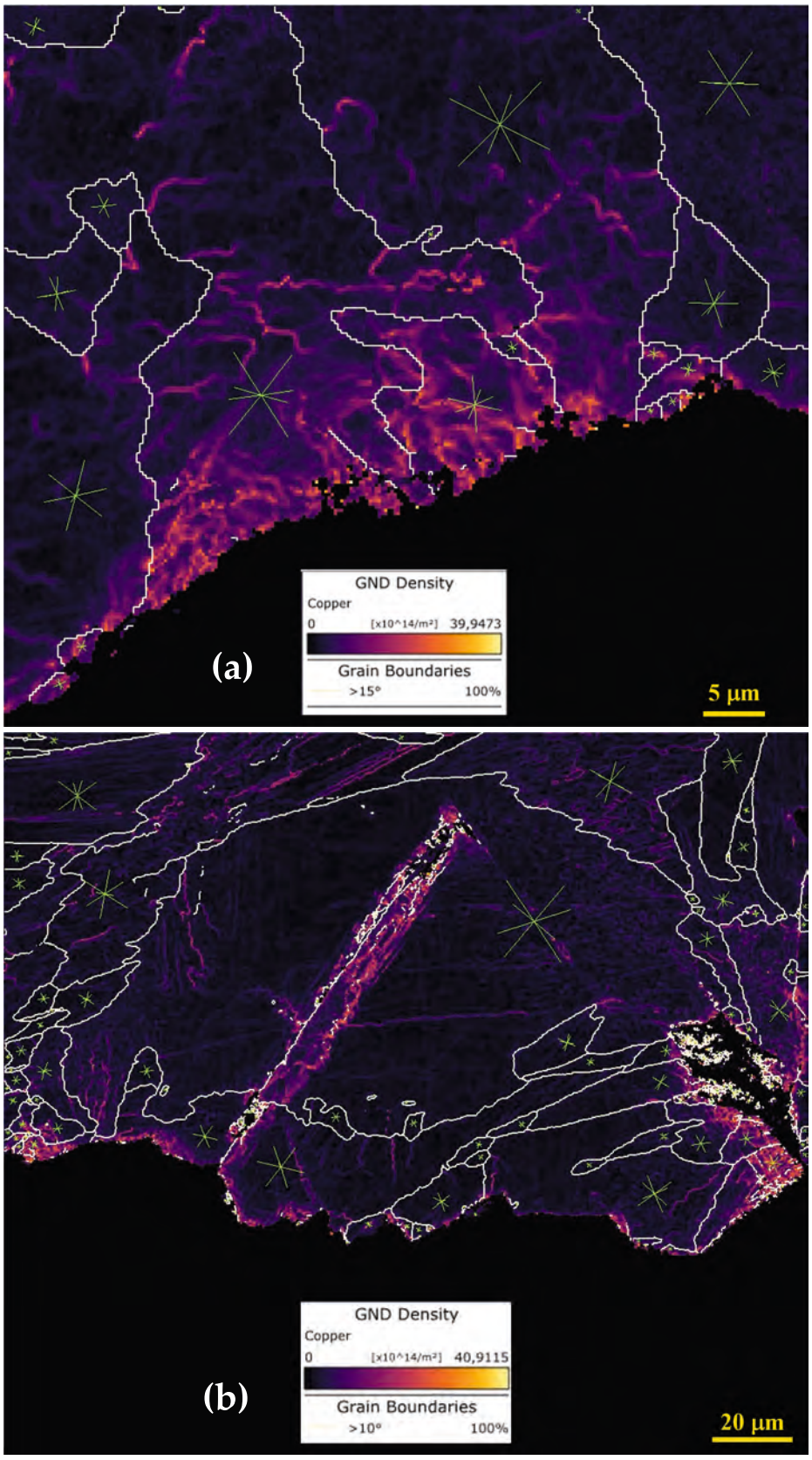

Fig. 19. Grain boundary and GND maps near the crack initiation region for horizontally printed a) HT specimen (F21: σ_a=241MPa & N_f=4.64×10^5 cycles) and b) AB specimen (F14: σ_a=222MPa & N_f=2.27×10^6 cycles).

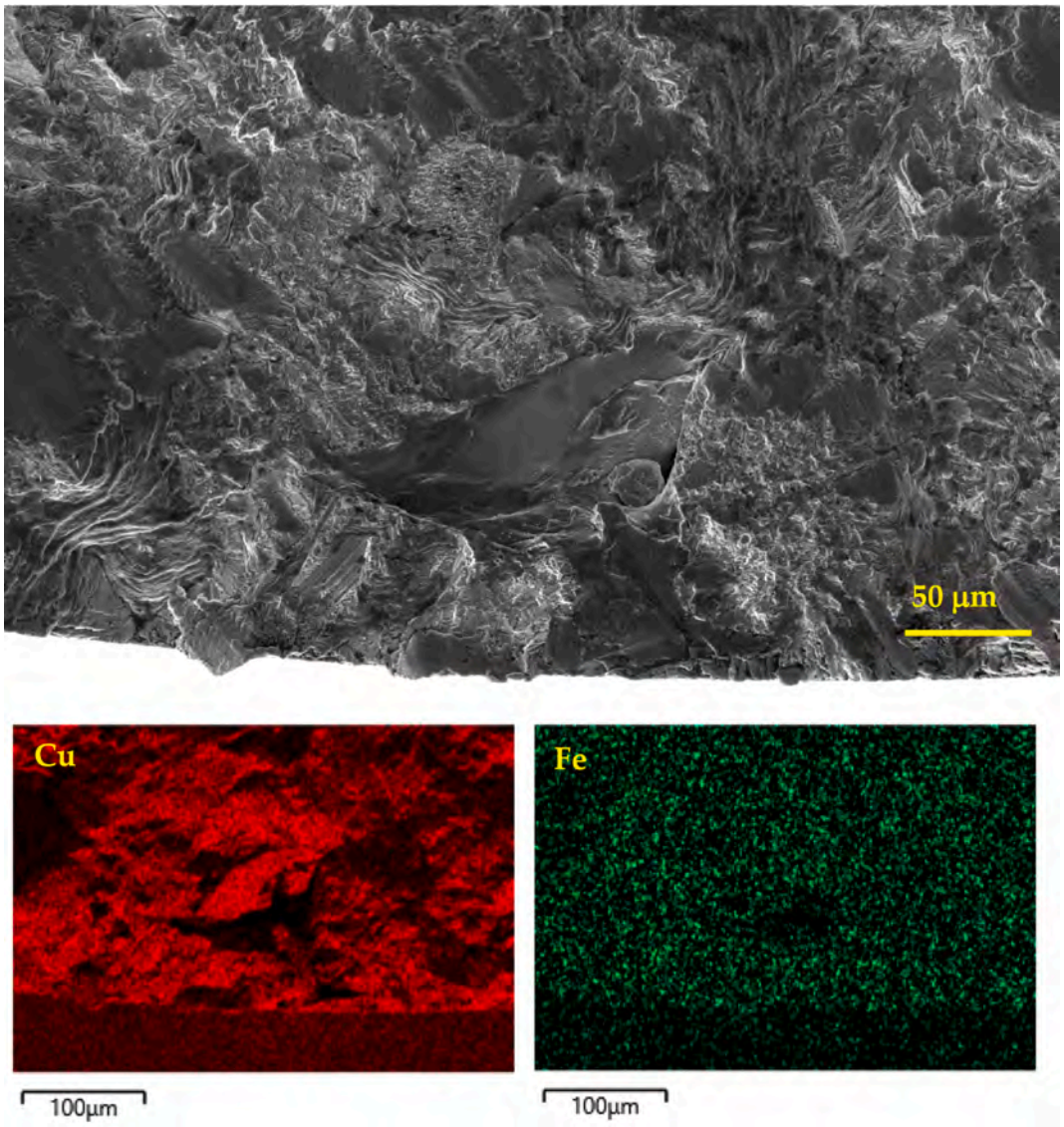

Fig. 20. EDS elemental map showing the distribution of elements on the fatigue fracture surface; (a) vertically printed AB, F21 (σ_a=222MPa and N_f=9.43×10^5 cycles), and (b) horizontally printed HT, F21 (σ_a=241MPa and N_f=4.64×10^5 cycles).

of the fatigue fracture surface, highlighting both the crack propagation zone and the final fracture zone. In the propagation region of most specimens, secondary cracks are observed, with a representative example shown in Fig. S4(a) for an AB vertically printed specimen (F7: σ_a = 241MPa and N_f=7.74×10^5 cycles). In the final fracture region, the morphology of all specimens is characterized by well-defined dimples (Fig. S4(b)). The presence of these dimples confirms that the final fracture occurred through a ductile failure mechanism after the fatigue crack propagation was completed. This indicates that the material underwent plastic deformation before ultimately failing.

Fig. S5 (Supplementary Materials) presents SEM images of the fracture surfaces for specimens in the AB condition, comparing horizontally printed and vertically printed specimens tested at the same stress level of 241MPa. These specimens showed relatively similar fatigue lives. In both orientations, fatigue striations are clearly visible near the middle of the fracture surface. Focusing on a representative region of the fracture surface, we counted ten striations. For the horizontally printed specimen (Fig. S5(a)), the total striation spacing was measured to be 7.79µm, corresponding to an average crack growth rate of 0.78µm per cycle. For the vertically printed specimen (Fig. S5(b)), the total spacing was 7.46µm, which corresponds to a crack growth rate of 0.75µm per cycle. These findings suggest that under the tested conditions, the crack growth behavior is relatively consistent and isotropic, showing minimal dependence on the build orientation.

To further investigate the local embrittlement responsible for the faceted features on the fracture surface, we conducted EDS analysis. Fig. 20 presents the EDS results for the fatigue fracture surfaces of both vertically (Fig. 20a) and horizontally (Fig. 20b) printed specimens. In both conditions, the primary matrix elements, Copper (Cu), Nickel (Ni), and Iron (Fe), are distributed uniformly, indicating a homogeneous base material. However, a significant co-localization of Niobium (Nb), Manganese (Mn), and Silicon (Si) is observed in specific areas. This strong elemental segregation suggests the presence of second-phase particles, likely hard precipitates (e.g., Nb-rich) or non-metallic inclusions (e.g., silicates). Metallurgically, these particles represent a discontinuity in the microstructure, leading to a significant mismatch in mechanical properties (high hardness/low ductility) compared to the surrounding matrix.

Under cyclic loading, these rigid particles weaken local strain compatibility, giving rise to severe stress concentrations at the

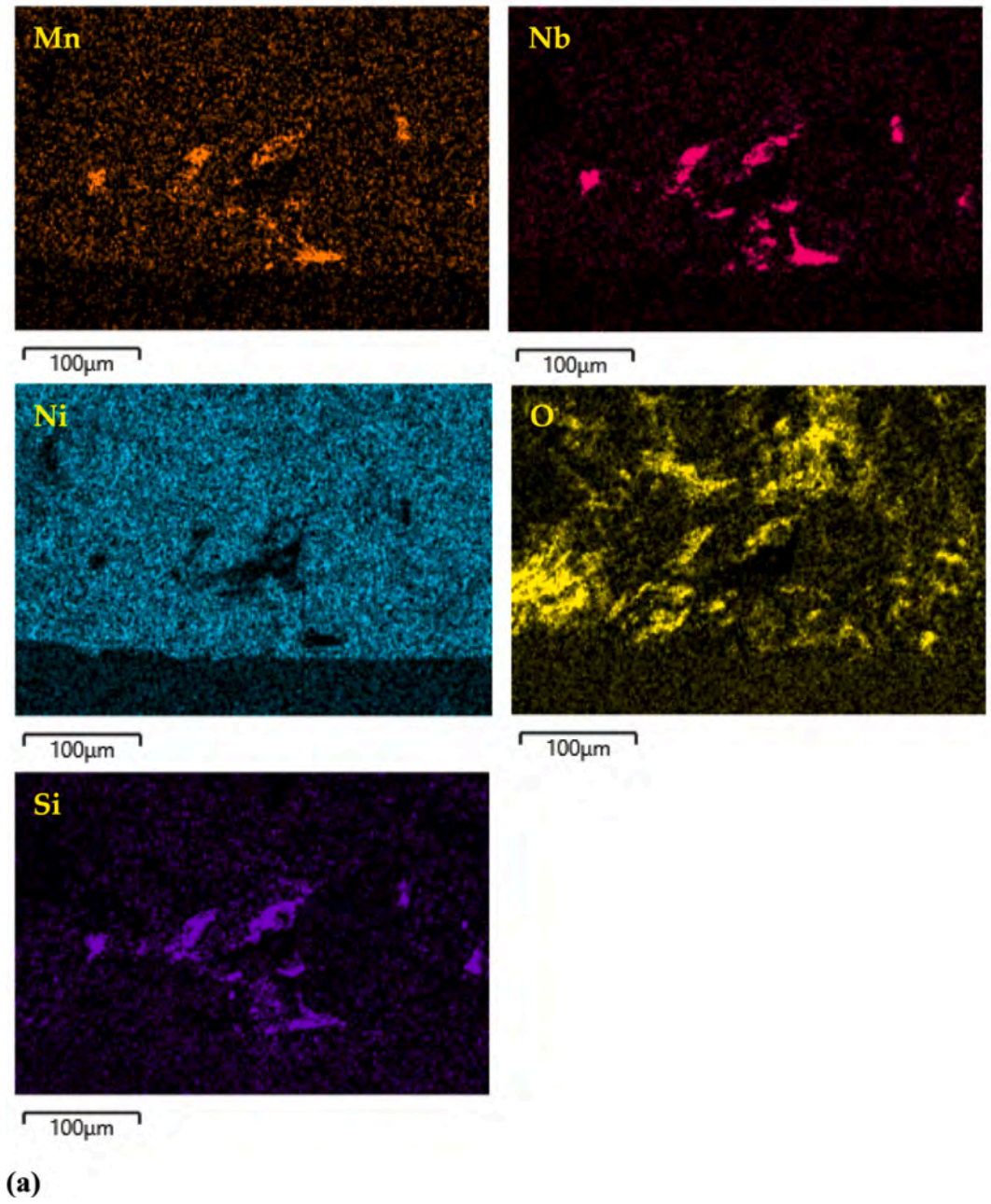

Fig. 20. (*continued*).

particle–matrix interfaces. This localized mechanical (e.g., stiffness) mismatch provides the initial conditions for crack nucleation. Importantly, these segregated regions also promote localized embrittlement, as the surrounding matrix becomes increasingly constrained and less capable of accommodating plastic deformation, leading to facet formation.

To characterize crack initiation at the facets, these features were treated as equivalent small cracks. Following Murakami's methodology [55–57], the characteristic dimension of these facets was defined by the square root of facet area ($\sqrt{area_{facet}}$). This definition allows the evaluation of the stress intensity factor (SIF) range, which was calculated as $\Delta K = Y\Delta\sigma\sqrt{\pi \times \sqrt{area_{eq}}}$, where the constant Y was set to 0.5, as all observed facets were classified as internal defects. The equivalent area ($\sqrt{area_{eq}}$), accounts for variations in material strength due to differences in printing direction (horizontal or vertical) and post-processing conditions (HT or AB). It was determined using the Murakami fatigue limit equation, which incorporates the Vickers hardness (HV) measured along the build direction as $\sqrt{area_{eq}} = \left(\frac{HV_{ref}+120}{HV_i+120}\right)^6 \sqrt{area_{facet}}$, where HV_{ref} is the reference Vickers hardness, taken as the hardness of the vertically printed HT condition, and HV_i is the hardness of the specific condition under evaluation (e.g., horizontally printed specimens). The hardness values utilized for the four investigated conditions are 252 for horizontally printed heat-treated, 189 for horizontally printed as-built, 241 for vertically printed HT, and 204 for vertically printed AB. By incorporating the specific facet dimensions at the initiation site into this equation, the local driving force for crack propagation was quantified.

Facet sizes ($\sqrt{area_{facet}}$) at crack initiation predominantly range from 50 to 100μm, with occasional smaller (~20μm) and larger (120–140μm) facets, comparable to the average grain size (~50μm), indicating that crack initiation is controlled by single grains or clusters of favorably oriented grains. Fig. S6 (Supplementary Materials) shows the semi-

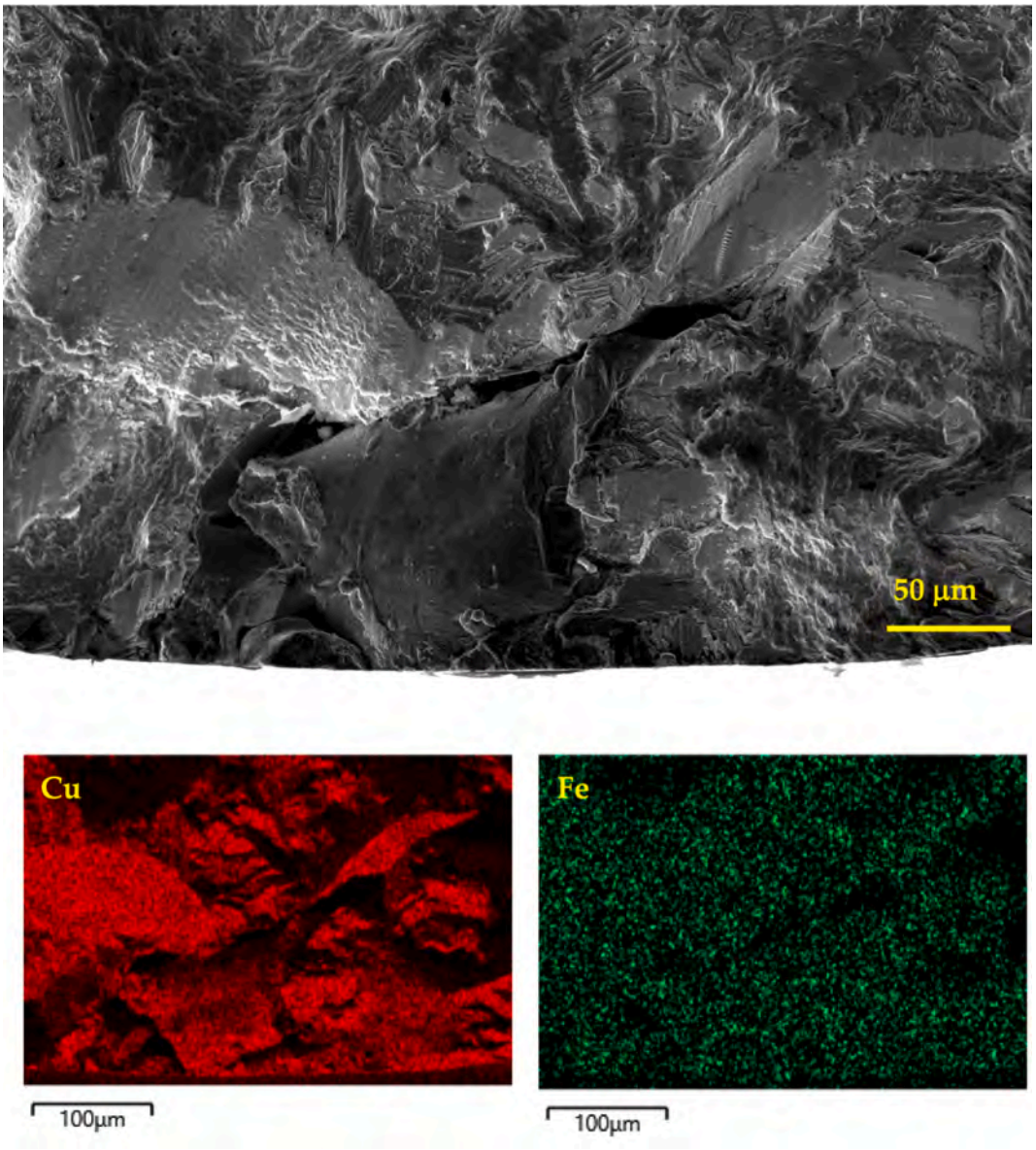

Fig. 20. (*continued*).

logarithmic correlation between the equivalent defect size ($\sqrt{area_{eq}}$) and the calculated ΔK. This relationship demonstrates that larger facets act as stronger stress concentrators, leading to higher local ΔK values under a constant applied stress and thereby increasing the driving force for fatigue crack propagation.

4. Conclusions

In the present work, the fully reversed uniaxial HCF behavior of PBF-LB 70/30 Cu–Ni alloy was investigated at room temperature in both AB and HT conditions, considering vertically printed and horizontally printed settings. Advanced characterization techniques were employed to establish correlations among microstructure, defects, mechanical properties, and fatigue performance of the studied material, and to quantify the governing crack-initiation mechanism(s). The key findings of this study are summarized as follows:

1. TEM analysis revealed a fine cellular substructure within the grains, characteristic of rapid solidification during PBF-LB. The α-phase solid solution was largely homogeneous, with HT reducing the Cu and Mn segregation at cell boundaries, and nanoscale SiO_2 inclusions were observed within grains and along cell boundaries in both AB and HT specimens.
2. Horizontally printed specimens exhibited higher YS and UTS but lower ductility than vertically printed specimens, with post-print HT further enhancing tensile strength and resulting in the highest strength in horizontally printed, heat-treated samples.
3. At higher stress amplitudes (>333MPa), horizontally printed HT specimens exhibited the longest fatigue lives, whereas vertically printed AB specimens showed the lowest fatigue performance. In contrast, at lower stress amplitudes (<333MPa), vertically printed HT specimens demonstrated superior fatigue resistance within this regime.
4. Fracture surface analysis revealed three main crack-initiation modes: direct initiation from process-induced defects, initiation on large crystallographic facets, and facet-assisted initiation near defects. Fatigue life was strongly influenced by the size and prominence of these features, with specimens containing smaller or less pronounced initiating sites exhibiting longer fatigue lives.

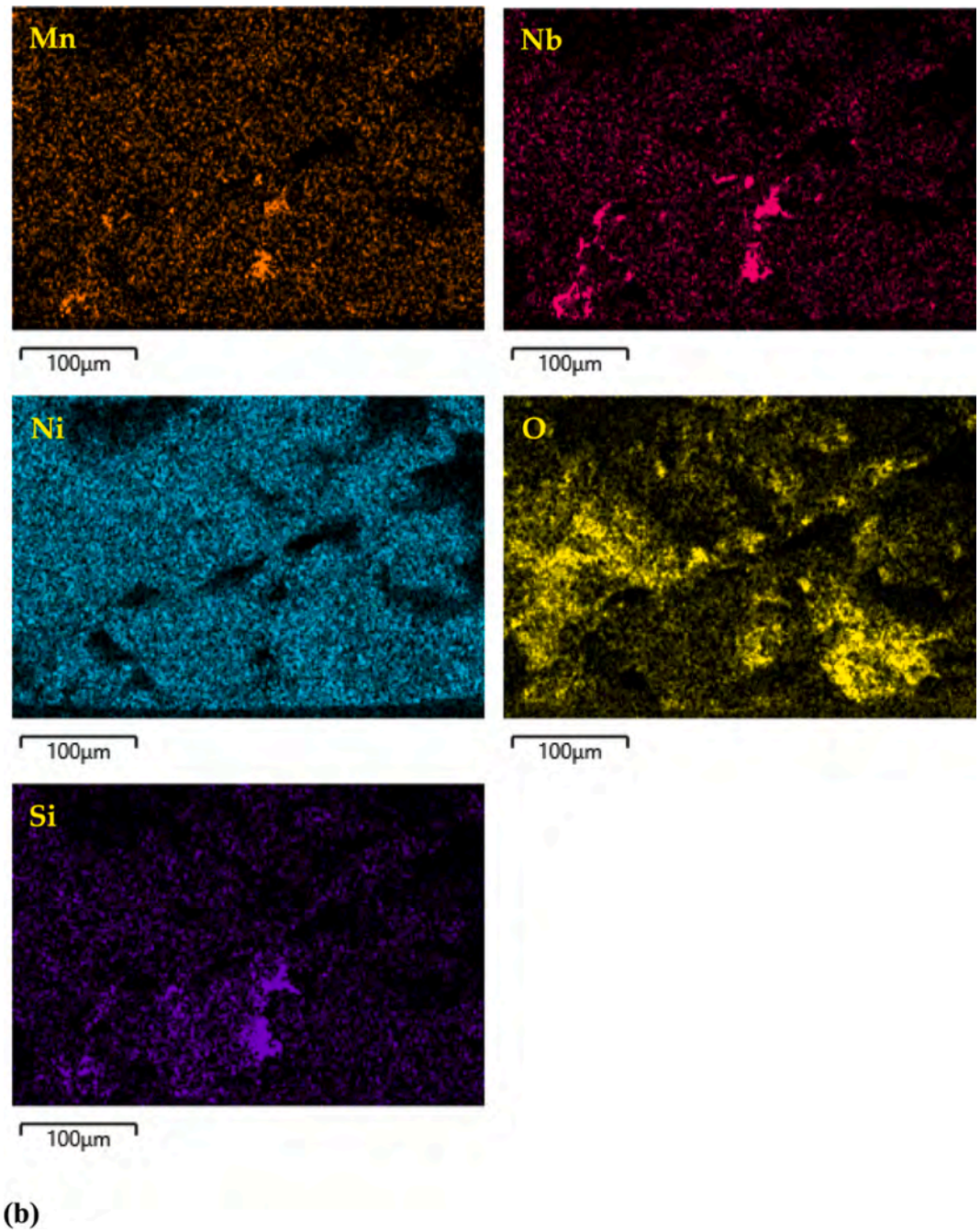

Fig. 20. (*continued*).

Overall, the fatigue behavior of PBF-LB 70/30 Cu–Ni is governed by a complex interplay of microstructural features, defect characteristics, and processing conditions. HT enhances fatigue resistance by relieving residual stresses and promoting precipitation strengthening, while surface and subsurface defects, facets, and elemental segregation act as primary sites for crack initiation. These findings provide critical insights for the design of fatigue-resistant PBF-LB Cu–Ni components in marine and naval applications.

The findings of this research on the ambient-air HCF behavior of machined PBF-LB 70/30 Cu–Ni provide, for the first time, essential baseline data and a clearer understanding of the dominant mechanisms governing fatigue crack initiation in this alloy system. Given the intended applications of PBF-LB 70/30 Cu–Ni alloys in marine and naval environments, our future work will focus on both in-situ and ex-situ corrosion-fatigue studies. Such efforts would enable a direct comparison between the corrosion-fatigue S–N response and the ambient-air S–N data reported herein, thereby quantifying the extent of fatigue-strength degradation associated with corrosive exposure. Moreover, these investigations would allow for a systematic evaluation of whether the controlling failure mechanisms observed in non-corroded (virgin) specimens persist in pre-corroded samples subjected to ex-situ corrosion fatigue, and how they may evolve under coupled corrosion–fatigue conditions in in-situ testing.

CRediT authorship contribution statement

Mojtaba Roshan: Writing – original draft, Methodology, Investigation, Formal analysis, Data curation. **MohammadBagher Mahtabi:** Writing – original draft, Methodology, Investigation, Formal analysis, Data curation. **Wiktor Bednarczyk:** Writing – review & editing,

Software, Methodology, Investigation. **Marta Gajewska:** Writing – review & editing, Visualization, Software, Methodology, Investigation. **Grzegorz Cios:** Software, Methodology, Investigation, Data curation. **Alessandro Benelli:** Visualization, Software, Methodology, Data curation. **Andrea Tridello:** Writing – review & editing, Software, Methodology, Formal analysis. **Zaynab Mahbooba:** Writing – review & editing, Validation, Resources, Project administration. **Ankit Saharan:** Resources, Project administration. **Meysam Haghshenas:** Writing – review & editing, Supervision, Resources, Project administration, Funding acquisition, Conceptualization.

Declaration of competing interest

The authors declare that they have no known competing financial interests or personal relationships that could have appeared to influence the work reported in this paper.

Acknowledgement

The corresponding author would like to acknowledge Professor Zachary Harris (University of Pittsburgh) for the XRF quantifications on the printed specimens.

Appendix A. Supplementary data

Supplementary data to this article can be found online at https://doi.org/10.1016/j.ijfatigue.2026.109574.

Data availability

Data will be made available on request.

References

[1] Vahedi Nemani A, Ghaffari M, Sabet Bokati K, Valizade N, Afshari E, Nasiri A. Advancements in additive manufacturing for copper-based alloys and composites: a comprehensive review. J Manuf Mater Process 2024;8(2):54.
[2] Bhatt B, Martucci A, Biamino S, Ugues D, Bondioli F, Montanaro L, et al. Current trends in electron beam and laser powder bed fusion additive manufacturing of copper alloys: Composition, defects, properties, and challenges. Mater Des 2025;113742.
[3] Javed MA, Neil WC, Wade SA. From defence to damage: the impact of seawater passivation on microbially influenced corrosion in CuNi 70/30 alloy. Environ Sci Water Res Technol 2024;10(11):2929–45.
[4] Larché N., Thierry D., Lang T. Internal Corrosion of Copper-Nickel Alloy Tubes 90/10 and 70/30 in Chlorinated Seawater for Shell and Tube Heat Exchangers. Corrosion 2019, March 24–28, 2019 Nashville, TN, Paper No: C2019-13338. https://doi.org/10.5006/C2019-13338.
[5] Nattah AM, Salim AM, Dawood NM. Influence of nano chromium addition on the corrosion and erosion–corrosion behavior of cupronickel 70/30 alloy in seawater. Open Eng 2023;13(1):20220491.
[6] Bharti A, Maharaja H, Sivaprasad S, Mishra S, Bhattacharyya A. Effect of Strain Amplitude on Low-Cycle Fatigue Deformation Behavior of a Cu-Ni Alloy. Mater Sci Eng A 2025;149401.
[7] Yadollahi A, Shamsaei N. Additive manufacturing of fatigue resistant materials: challenges and opportunities. Int J Fatigue 2017;98:14–31.
[8] Martucci A, Aversa A, Lombardi M. Ongoing challenges of laser-based powder bed fusion processing of Al alloys and potential solutions from the literature—a review. Materials 2023;16(3):1084.
[9] Butt MM, Laieghi H, Kvvssn V, Uddin Z, Shah M, Ansari P, et al. Fatigue performance in additively manufactured metal alloys. Prog Addit Manuf 2025;10(4):1809–41.
[10] Foteinopoulos P, Papacharalampopoulos A, Stavropoulos P. On thermal modeling of Additive Manufacturing processes. CIRP J Manuf Sci Technol 2018;20:66–83.
[11] Li C, Liu ZY, Fang XY, Guo YB. Residual stress in metal additive manufacturing. Procedia CIRP 2018;71:348–53.
[12] Antu MNR, Shakil SI, Bednarczyk W, Gajewska M, Mahbooba Z, Saharan A, Haghshenas M. Strength-hardness Correlation in a Laser Powder Bed Fused Scandium-free Al-Mg-Zr Alloy. Progr Eng Sci 2025:100052.
[13] James MN, Hughes DJ, Chen Z, Lombard H, Hattingh DG, Asquith D, et al. Residual stresses and fatigue performance. Eng Fail Anal 2007;14(2):384–95.
[14] Smudde CM, San Marchi CW, Hill MR, Gibeling JC. Effects of residual stress on orientation dependent fatigue crack growth rates in additively manufactured stainless steel. Int J Fatigue 2023;169:107489.
[15] Gordon JV, Haden CV, Nied HF, Vinci RP, Harlow DG. Fatigue crack growth anisotropy, texture and residual stress in austenitic steel made by wire and arc additive manufacturing. Mater Sci Eng A 2018;724:431–8.
[16] Blinn B, Krebs F, Ley M, Teutsch R, Beck T. Determination of the influence of a stress-relief heat treatment and additively manufactured surface on the fatigue behavior of selectively laser melted AISI 316L by using efficient short-time procedures. Int J Fatigue 2020;131:105301.
[17] Brennan MC, Keist JS, Palmer TA. Defects in metal additive manufacturing processes. Springer; 2021.
[18] Laleh M, Hughes AE, Yang S, Wang J, Li J, Glenn AM, et al. A critical insight into lack-of-fusion pore structures in additively manufactured stainless steel. Addit Manuf 2021;38:101762.
[19] Huang R, Shi W, Xu K, Wang R, Chen X, Xie H, et al. The influence of laser energy density on the low cycle fatigue behavior for laser powder bed fused tantalum. Int J Fatigue 2025;109301.
[20] Biswal R, Syed AK, Zhang X. Assessment of the effect of isolated porosity defects on the fatigue performance of additive manufactured titanium alloy. Addit Manuf 2018;23:433–42.
[21] Mahtabi M, Roshan M, Shakil SI, Tridello A, Paolino DS, Bednarczyk W, et al. Crack initiation, small crack growth, and stress intensity factor in the very high cycle fatigue (VHCF) of wire arc additive manufactured (WAAM) nickel aluminum bronze (NAB). Eng Fract Mech 2025;313:110671.
[22] Sanaei N, Fatemi A. Defects in additive manufactured metals and their effect on fatigue performance: a state-of-the-art review. Prog Mater Sci 2021;117:100724.
[23] Huang R, Xie H, Guo L, Cai X, Yang X, Wei K. High cycle fatigue behavior and strengthening mechanisms of laser powder bed fusion pure tantalum. Int J Fatigue 2025;190:108624.
[24] Yadollahi A, Shamsaei N, Thompson SM, Elwany A, Bian L. Effects of building orientation and heat treatment on fatigue behavior of selective laser melted 17-4 PH stainless steel. Int J Fatigue 2017;94:218–35.
[25] Dixit S, Liu S, Murdoch HA, Smith PM. Investigating build orientation-induced mechanical anisotropy in additive manufacturing 316L stainless steel. Mater Sci Eng A 2023;880:145308.
[26] Zhao J, Easton M, Qian M, Leary M, Brandt M. Effect of building direction on porosity and fatigue life of selective laser melted AlSi12Mg alloy. Mater Sci Eng A 2018;729:76–85.
[27] Shrestha R, Simsiriwong J, Shamsaei N. Fatigue behavior of additive manufactured 316L stainless steel parts: Effects of layer orientation and surface roughness. Addit Manuf 2019;28:23–38.
[28] Meneghetti G, Rigon D, Gennari C. An analysis of defects influence on axial fatigue strength of maraging steel specimens produced by additive manufacturing. Int J Fatigue 2019;118:54–64.
[29] Uddin Z, Butt MM, Kvvssn V, Salamci MU, Kizil H. Understanding the Effects of Manufacturing Attributes on damage Tolerance of Additively Manufactured Parts and Exploring Synergy among Process-Structure-Properties. a Comprehensive Review. Eng Rep 2024;6(11):e13020.
[30] Nadimi M, Song J, Cheng L, Fu Y. Corrosion evaluation and microstructural characteristics of 70/30 copper-nickel alloy fabricated by laser powder bed fusion. J Alloys Metall Syst 2025;9:100155.
[31] Liu Z, Zhang Q, Zhang B, Wang Y, Zuo P, Zhang Z, et al. Investigation on mechanical properties and corrosion behavior of laser powder bed fusion 70/30 copper-nickel alloy. Corros Sci 2024;232:112040.
[32] Gao S, Zhang M, Ding J, He X, Chen H, Zhou S. Tailoring the microstructure and mechanical properties for additive manufactured CuNi30 alloy via in-situ NbC formation. Mater Lett 2025;138714.
[33] Anjum MA, Nath A, Goel S, Mäkilä E, Sarkar S, Salminen A, et al. Tribocorrosion Performance of Additively Manufactured CuNi30 and SS-316L in Marine Environments: Seawater Resistant Alloys. J Mater Res Technol 2025.
[34] Roshan M, Mahtabi M, Bednarczyk W, Gajewska M, Cios G, Mahbooba Z, et al. Powder Bed Fused–Laser Beam (PBF-LB) 70/30 Copper-Nickel (Cu-30Ni): Hierarchical Microstructure and Mechanical Properties. J Alloy Compd 2025;183312.
[35] Sudarshan TS, Louthan MR, Place TA, Mabie HH. Hydrogen and humidity effects on fatigue behavior of a 70–30 copper-nickel alloy. J Mater Energy Syst 1986;8(3):291–6.
[36] Norkett JE, Fisher CR. Temperature-Dependent Material Property Database of cast 70/30 Cu-Ni Material. Integrating Materials and Manufacturing Innovation 2025:1–12.
[37] ASTM B369-09 . Standard Specification for Copper-Nickel Alloy Castings ; 2016. https://store.astm.org/b0369-09r16.html.
[38] ASTM E466: Standard Practice for Conducting Force Controlled Constant Amplitude Axial Fatigue Tests of Metallic Materials, 2021.
[39] B. Beausir, J.J. Fundenberger. Analysis Tools for Electron and X-ray diffraction, ATEX-software, www. Université de Lorraine-Metz 201(7); 2017. atex-software.eu.
[40] ASTM E8/E8M-22. In: Standard Test Methods for Tension Testing of Metallic Materials; 2024. https://store.astm.org/e0008_e0008m-22.html.
[41] Fallah V, Amoorezaei M, Provatas N, Corbin SF, Khajepour A. Phase-field simulation of solidification morphology in laser powder deposition of Ti–Nb alloys. Acta Mater 2012;60(4):1633–46.
[42] Sohrabpoor H, Salarvand V, Lupoi R, Chu Q, Li W, Aldwell B, et al. Microstructural and mechanical evaluation of post-processed SS 316L manufactured by laser-based powder bed fusion. J Mater Res Technol. 2021;12:210–20.
[43] Sun W, Ma Ye, Li P, Moumni Z, Zhang W. Effects of build direction and heat treatment on the defect characterization and fatigue properties of laser powder bed fusion Ti6Al4V. Aerospace 2024;11(10):854.

[44] Ronneberg T, Davies CM, Hooper PA. Revealing relationships between porosity, microstructure and mechanical properties of laser powder bed fusion 316L stainless steel through heat treatment. Mater Des 2020;189:108481.
[45] Karakaş Ö, Kardeş FB, Foti P, Berto F. An overview of factors affecting high-cycle fatigue of additive manufacturing metals. Fatigue Fract Eng Mater Struct 2023;46 (5):1649–68.
[46] Liu H, Yu H, Guo C, Chen X, Zhong S, Zhou L, et al. Review on fatigue of additive manufactured metallic alloys: microstructure, performance, enhancement, and assessment methods. Adv Mater 2024;36(17):2306570.
[47] Javidrad H, Koc B, Bayraktar H, Simsek U, Gunaydin K. Fatigue performance of metal additive manufacturing: a comprehensive overview. Virt Phys Prototyp 2024;19(1):e2302556.
[48] Ono Y, Yuri T, Sumiyoshi H, Takeuchi E, Matsuoka S, Ogata T. High-cycle fatigue properties at cryogenic temperatures in Inconel 718 nickel-based superalloy. Mater Trans 2004;45(2):342–5.
[49] Chu Z, Jinjiang Y, Xiaofeng S, Hengrong G, Zhuangqi H. High temperature low cycle fatigue behavior of a directionally solidified Ni-base superalloy DZ951. Mater Sci Eng A 2008;488(1–2):389–97.
[50] Sun C, Li W, Li C, Sun R, Liu G, Li X. Study on microstructure and fatigue properties of laser powder bed fusion nickel-based superalloy with heat treatment. Add Manufact Front 2025:200217.
[51] Ma X-F, Duan Z, Shi H-J, Murai R, Yanagisawa E. Fatigue and fracture behavior of nickel-based superalloy Inconel 718 up to the very high cycle regime. Journal of Zhejiang University-Science A 2010;11(10):727–37.
[52] Yu X, Lin X, Wang Z, Zhang S, Gao X, Zhang Y, et al. Room and high temperature high-cycle fatigue properties of Inconel 718 superalloy prepared using laser directed energy deposition. Mater Sci Eng A 2021;825:141865.
[53] Wu Z, He Z, Wu S, Gao X, Lei L, Liu C, et al. Rotating bending fatigue mechanisms of L-PBF manufactured Ti-6Al-4V alloys using in situ X-ray tomography. Int J Fatigue 2023;176:107876.
[54] Nandi I, Soman S, Molaei R, Tilson W, Shamsaei N, Shao S. Competing role of volumetric defects and microstructure on the fatigue behavior of additively manufactured Inconel 718: an experimental study. Int J Fatigue 2026;109486.
[55] Murakami Y. Metal fatigue: effects of small defects and nonmetallic inclusions. Academic Press; 2019.
[56] Murakami Y, Endo M. Effects of hardness and crack geometries on delta k sub th of small cracks emanating from small defects. The Behaviour of Short Fatigue Cracks: Mechanical Engineering Publications; 1986. p. 275–93.
[57] Murakami Y, Kodama S, Konuma S. Quantitative evaluation of effects of non-metallic inclusions on fatigue strength of high strength steels. I: basic fatigue mechanism and evaluation of correlation between the fatigue fracture stress and the size and location of non-metallic inclusions. Int J Fatigue 1989;11(5):291–8.